Durability of Advanced Woven Polymer Matrix Composites for Aerospace Applications

Sneha Ramesh Patel

Thesis submitted to the Faculty of the
Virginia Polytechnic Institute and State University
in partial fulfillment of the requirements for the degree of

Master of Science
in
Engineering Mechanics

Scott W. Case, Chair
Kenneth L. Reifsnider
John J. Lesko

June 16, 1999
Blacksburg, Virginia

Keywords: Composites, Woven, Fatigue, Environmental, Durability

DURABILITY OF ADVANCED WOVEN COMPOSITES IN AEROSPACE APPLICATIONS

Sneha Ramesh Patel

(ABSTRACT)

The objective of this project was to evaluate and model the effects of moisture, temperature, and combined hygrothermal aging on the durability of a graphite/epoxy woven composite material system. Imposed environmental and aging conditions were considered to be representative of service conditions for the engine of an advanced subsonic aircraft for which the composite system is a candidate material. The study was designed such that the results could be used in a residual strength based life prediction approach that accounted for both the mechanical fatigue and environmental conditions. Damage mechanisms and failure modes were determined through fatigue testing, residual strength testing, and nondestructive evaluation. The experimental data generally revealed little effect of environment on strength degradation during fatigue despite notable differences in damage accumulation processes.

Modeling efforts were concentrated on initial stiffness, moisture uptake, and residual strength prediction, where the results from the first two efforts were intended to generate inputs for the life prediction. The Ishikawa and Chou fiber undulation and bridging model [22] was shown to provide an accurate stiffness prediction and was subsequently used in parametric studies to determine the effect of weave architecture and geometry. A moisture uptake model developed by Roy [16] for laminates containing single direction

cracks was extended to predict moisture uptake in laminates containing cracks in directions parallel and transverse to the loading direction. The life prediction approach was based on ideas developed by Reifsnider and colleagues [36,37,43]. The intention in this case was to use the critical element paradigm to predict the combined effects of alternating environmental (temperature and moisture) conditions imposed during fatigue. Since experimental results indicated that temperature and moisture did not significantly affect the strength and life of the material, a successful life prediction analysis was performed as a function of only fatigue stress level and cycles.

Dedication

This thesis is dedicated to the author’s parents and to James who all provided endless support in every way.

Acknowledgements

The author would like to thank:

- Dr. Scott Case for generously giving of his guidance, patience, and time and for providing many opportunities to grow and learn
- Dr. Ken Reifsnider and Dr. Jack Lesko for taking the time to serve on my committee
- Pratt and Whitney, particularly technical monitors Dr. Rajiv Naik and Ron Cairo, for sponsoring this project
- Virginia Space Grant Consortium for additional funding
- Howard Halverson and Nikhil Verghese for teaching me so much and helping me in more ways than I could name
- Austin Smith for his hard work with any given task, no matter how tedious
- Shelia Collins for making sure everything got to where it was going when it needed to get there
- The MRG as a whole for making my time working with the group very enjoyable as well as educational

Table of Contents

Table of Figures

List of Tables

Chapter 1 Introduction

1.1 Background and Motivation

In the past twenty years, the use of composite materials in the aircraft industry, among others, has grown immensely. Composite systems offer an advantage over traditional aircraft materials (metals) because they tend to exhibit higher strength/weight and stiffness/weight ratios than metals, thus making the aircraft lighter and improving performance. Woven composites are increasingly considered for such applications because they offer ease in manufacturing of complicated geometries, but the durability (strength and life) of the material is even less well characterized than that of non-woven (angle-ply) laminates. Moreover, aircraft components, particularly in the engine, are subject to environmental attack in the form of high temperatures, excessive humidity, etc. Even though temperature and moisture are known to affect fiber/matrix stress distributions and matrix properties, the exact nature of the effect of such conditions on the durability of any specific material, particularly woven materials, is generally not understood.

Pratt and Whitney is currently considering a woven graphite/epoxy composite material system for use in the engine of an advanced subsonic aircraft. An idealization of the service conditions for this engine is given in the representative mission profile shown in Figure 1. As can be imagined, industry has a direct benefit in durability studies which provide the robust knowledge of material behavior needed to make sound material selection choices.

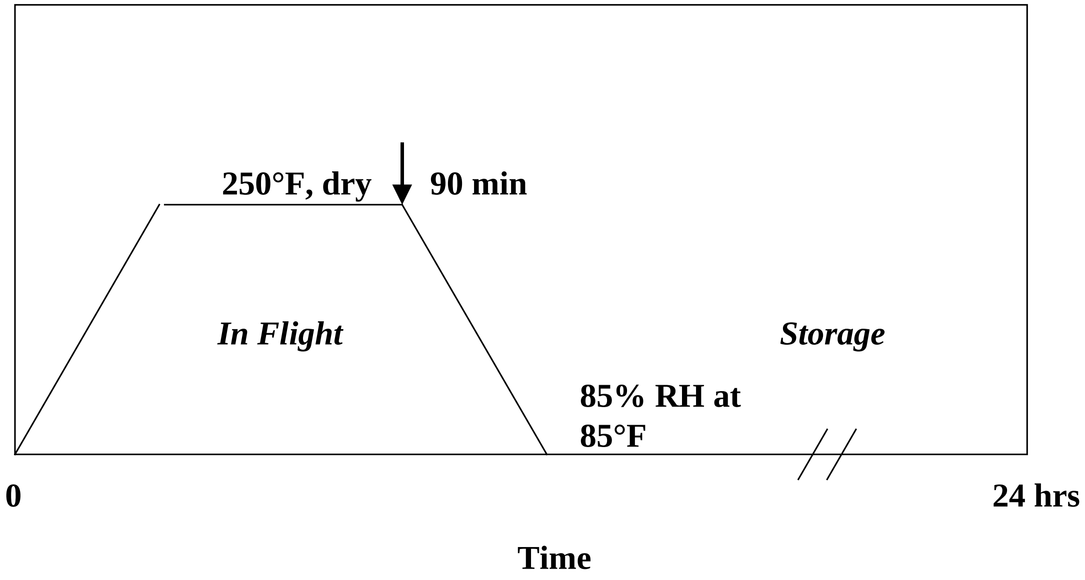

Figure 1: Mission cycle hygrothermal profile

Durability studies involve the investigation into the way in which the strength and structural integrity of materials evolve with mechanical loading and/or environmental conditions. Since environment can play a significant role in the fatigue process, such studies must be conducted under realistic environmental conditions. The results can provide the information necessary to assess in-field component integrity and develop analytical models to predict material behavior as a function of service parameters, significantly reducing the time and expense involved in the material selection process.

1.2 Project Objectives

As a consequence of the concerns discussed above, Pratt and Whitney has sponsored the current project with the following objectives:

- To evaluate the effects of moisture (85% RH at 85°F), temperature (250°F), and aging on the residual strength and life and damage tolerance of an AS4/PR500 (graphite/epoxy) five harness satin weave composite material system. Such an evaluation involves the determination of damage and failure modes through fatigue testing, residual strength testing, and nondestructive evaluation. The nature of the aging involved cycling the material through the hygrothermal profile of the mission cycle as shown in Figure 1 (i.e., the material was stored under the humidity condition except for once a day for ninety minutes when the temperature was ramped to 250°F).
- To use the results of the above proposed study to develop a residual strength based life prediction approach as a function of material and service parameters. This effort involves not only the major task of modeling the residual strength changes of the material, but also the sub-tasks of developing models to obtain inputs for the larger model, i.e. initial properties, moisture diffusion, etc.
- To validate the life prediction approach with experimental data.

1.3 Thesis Outline

The remainder of this thesis is organized as follows:

- Chapter 2 includes a literature review designed to provide a summary of the base of knowledge already available involving the issues of interest
- Chapter 3 includes a detailed description of the experimental testing involved and a discussion of the subsequent results
- Chapter 4 discusses the philosophy and application of the analytical models considered

- Chapter 5 provides a summary of the conclusions drawn from both the experimental and analytical efforts as well as a discussion on the work recommended for the future.

Chapter 2 Literature Review

The purpose of this literature review is to provide background information on the issues to be considered in this thesis and to emphasize the relevance of the present study. The topics covered in the review include 1) fatigue damage mechanisms in woven composites, 2) the effects of temperature and moisture on graphite/epoxy composites, 3) modeling of initial tensile properties of woven materials, and 4) life prediction of composite materials.

2.1 Woven Composite Fatigue

In order to effectively study the fatigue behavior of any composite material system, we must consider the damage accumulation that occurs as a result of the fatigue process. Specifically, these damage mechanisms usually involve matrix cracking, fiber matrix debonding or delamination, and fiber breakage. Much work in the determination of fatigue damage mechanisms has been conducted on unidirectional and cross-ply laminates. However, while damage processes in multi-directional and orthotropic laminates are fairly well understood, those concepts cannot be strictly applied to woven composites because each woven ply is in and of itself bi-directional. Due to the relatively recent advent and use of woven fabric composites, only some of the more recent effort has concentrated on fatigue of woven materials.

Fujii et al. [1] discuss tensile fatigue damage mechanisms in a plain-weave glass fiber composite. The fatigue process of the composite was found to have three stages: 1) rapid modulus decay with cycles, 2) gradual modulus decay with cycles, and 3) another rapid modulus decay for the last few cycles. Thus, the stiffness reduction during fatigue of the woven material appeared to have the regions of damage as described by Reifsnider et al. [2] and shown in Figure 2.

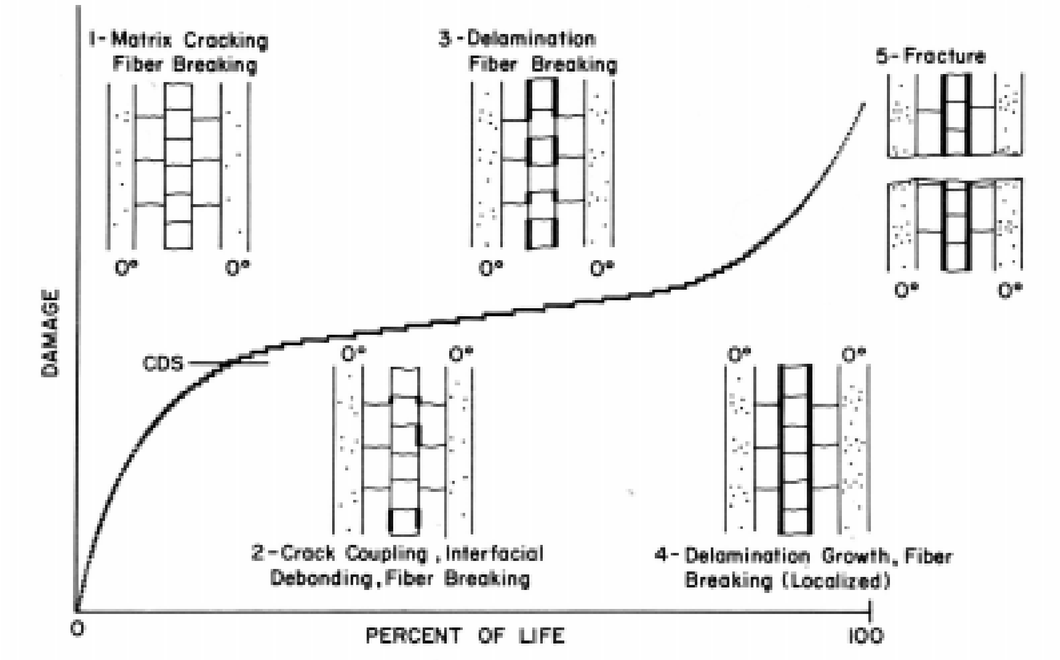

Figure 2: Damage progression during fatigue life [2]

However, while the stiffness curves of the woven materials appeared to be similar to that of angle-ply laminates, the events causing the stiffness changes differed somewhat. From experimental observations, the authors hypothesize that the damage progressed in the following way. The rapid modulus decay at the beginning of the fatigue process was caused by the initiation and accumulation of debonds in the weft and matrix cracks. This behavior is similar to that commonly observed in orthotropic laminates; however, the woven system behavior differs in that the debonds occur at each region surrounding a fiber undulation. Matrix cracking and weft debonding was observed to stop progressing after the cycle-life ratio (n/N) reached about 0.1. The cessation of the matrix cracking is in line with the characteristic damage state (CDS), described by Reifsnider et al. [3], commonly found to occur in multi-directional composites. However, the woven composites again differ in that such a damage state occurs at each of the cross-over points, as opposed to the global CDS in monotape composites. Thus, the authors have deemed each CDS to be a "meta-CDS". In the second fatigue stage, the gradual modulus decay is attributed to debonds starting to occur in the warp and "meta-delaminations" (small delaminations between warp and weft fiber bundles) occurring at the fabric cross-over points. From experimental results, the authors observed weave pitch of the fabric to be a parameter of meta-delamination because the meta-delamination and weft debonds occur at each cross-over point. This is somewhat similar to angle-ply laminates in which interior delaminations tend to occur where cracks intersect each other and where cracks meet fibers from adjacent plies.

Finally, Fujii et al. [1] claim that woven composites have unit areas of damage accumulation, or unit cells as shown in Figure 3, which can be used as parameters describing fatigue accumulation. This idea represents a departure from multi-directional laminates which have progressive damage accumulation from ply to ply. The authors go on to consider the possibility that many damaged unit cells are produced everywhere within the specimen in the middle stage where the gradual modulus decay represents the sum of fatigue damage of unit cells having different damage accumulations. Thus, the unit cell can be considered to be the representative volume element of the material system and will be further discussed in Section 3.1.

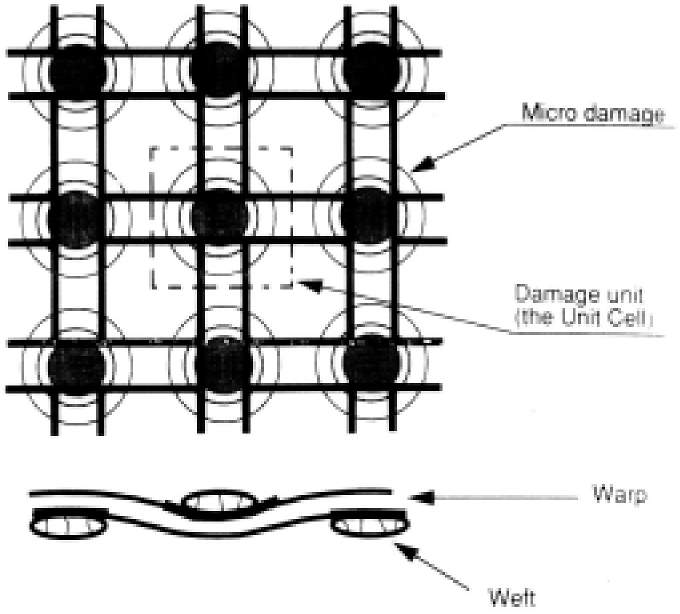

Figure 3: Unit cell of damage for a plain-woven composite [1]

Takemura and Fujii [4] discussed strength and stiffness reductions in a typical plain-woven CFRP (carbon fiber reinforced polymer) subjected to tension-tension fatigue. They observed excessive scatter (Figure 4) in the S-N curve, which was relatively flat. The material exhibited a high endurance limit with a fatigue strength of 80 to 85%. In addition, very little reduction in strength was found to occur for this material. Thus, the authors concluded that residual strength could not be used as a good indicator of the degree of fatigue damage for the PW-CFRP. The authors claim that the debonding between warp and weft bundles with cycling may explain the apparent unwavering of residual strength in that debonding may relax the residual stress in the thickness direction, causing the residual strength to increase. While this result does not bode well for the residual strength life prediction approach considered in the present study, the differences in material (different fiber and matrix) and the possible influence of environment should be kept in mind.

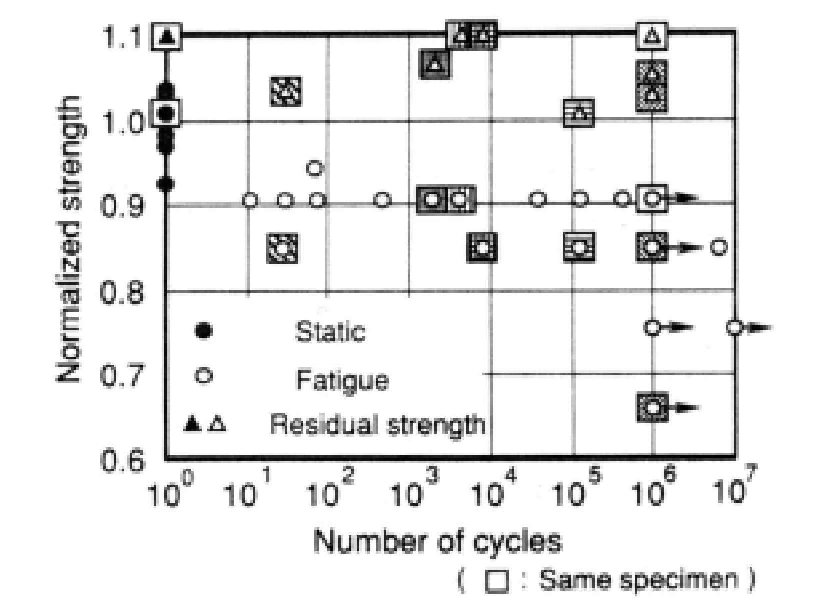

Figure 4: CFRP fatigue life and residual strength data from [4]

In looking at stiffness reduction with cycles, the authors found that for specimens with shorter fatigue lives, there was no apparent change in stiffness. In addition, the extent and path of the stiffness reduction was not found to be consistent for specimens fatigued at the same stress and for the same number of cycles. The number of cycles at which the stiffness started to decrease was found to depend on the stress level and increase as the stress level decreased. A maximum stiffness degradation of 3-4% was found for applied stress levels lower than the endurance limit. Consequently, stiffness reduction was also found to be a poor indicator of fatigue damage.

Since the weave architecture appears to play a significant role in the fatigue damage processes of woven composites, other weave patterns should also be considered. Cler [5] studied the fatigue behavior of five harness satin weave composite systems slated for use in an aircraft propulsion system. The author performed tension-tension fatigue cycling (R = 0.1, f = 10 Hz) at room temperature for two different balanced weaves: $[0/90]_{8w}$ and $[0/45/45/0]_s$. From micrograph images, the author determined that failed fatigue specimens exhibited predominant fiber pullout, indicating interface failure, and static specimens exhibited a cohesive rupture type failure. These observations prompted the conclusion that, for woven fabric laminates, static failures are fiber dominated and fatigue failures are resin and interface dominated. This is an important point when studying the effects of environment on the fatigue behavior of composites since the resin and interface are more prone to environmental attack than the fibers.

With regards to damage mechanisms, the author found that damage occurred early in the $[0]_8$ laminates and consisted of 90° cracks followed by delamination. In addition, it was observed that the rate of stiffness reduction due to fatigue damage increased with increasing fatigue stress levels. In this case, the author found no CDS in terms of the matrix cracking, but instead found that the crack density increased with fatigue life. Finally, Cler [5], like the authors mentioned previously, found the warp/fill crossover points to be “weak points” and susceptible to delamination. Indeed, through three-dimensional finite element analysis of plain weave composites, Whitcomb [6] found these areas to have large strain concentrations when uniaxial load is applied.

Thus, while the fatigue behavior of woven composite systems appears to be well outlined by the papers discussed above, the details of the processes and resulting property degradation are highly material dependent. In addition, the effects of environment on the fatigue behavior of woven systems remain to be considered.

2.2 Effects of Environment on Graphite/Epoxy Composites

In many cases, polymer composites are used in harsh environments because of their chemical and moisture resistance properties. When evaluating the utility of a composite material for a potential practical application, the behavior of the composite under the intended service conditions must be considered. To this end, many studies have focused on the effects of temperature and moisture on the mechanical behavior of a variety of composite material systems.

2.2.1 Moisture/Hygrothermal Effects

It is well known that moisture can degrade mechanical properties of polymer matrix composites (PMC's), especially at elevated temperature. In a survey of literature (that extended to 1982) on the effects of hygrothermal conditioning in fibrous composites, Weitsman [7] found the following major conclusions:

1) If a moisture saturation level exists, it depends heavily on relative humidity and less on temperature.
2) Moisture diffusivity is highly sensitive to temperature
3) Moisture enhances creep under external loads
4) Moisture induces swelling strains that can lead to internal stresses

5) Moisture lowers glass transition temperature of PMC's and may therefore affect the behavior of composites in hot, wet environments
6) Moisture causes a degradation of shear and compression properties

The above findings, while generally true, may of course vary in their accuracy depending on the material system, exact aging conditions, and time periods involved.

For example, a testament to the fact that we still lack understanding as to how, exactly, properties such as glass transition temperatures (T_g) may be affected by moisture is given by Zhou and Lucas [8]. The authors conducted moisture diffusion studies at 45°C, 60°C, 75°C, and 90°C where the specimens were immersed in water. They found that the T_g's of all water saturated samples decreased with *decreasing* water bath temperature. In most cases, the T_g's were fully recovered after sufficient drying. It was observed by the authors that these differences in T_g contradicted the findings of past investigators (e.g., [9]), who reported that T_g is controlled by water content and that samples with similar water contents should have similar T_g's. Zhou and Lucas [8] explained their differences in T_g by distinguishing between "chemioabsorbed" water and "physioabsorbed" water. Physioabsorbed water was described to be associated with weak Van der Waals bonding, which decreases the T_g. Chemioabsorbed water involves water strongly bonded to hydrophilic groups in the resin and enhances the T_g. The value for T_g was said to be affected by the distribution of chemioabsorbed water versus the physioabsorbed water in the material.

Pipes et al. [10] developed a method to analyze moisture and temperature induced stresses in a composite laminate. The method is principally based on classical laminated plate theory and assumes that an integrable moisture transport equation, such as the classical diffusion equation, may be found. Analyses of a $[0/+45/-45]_s$ six ply graphite/epoxy system showed that, for absorption, the outer layers of the composite were in compression, while inner layers were in tension. Shear stresses were zero in the outer layers, but significantly high in the inner layers, giving way to the possibility of high interlaminar shear stresses at laminate discontinuities. Upon desorption, exactly the opposite was predicted – large, compressive stresses in the inner layers and tensile stresses in the outer layers for early times. For long times, all stresses went to zero. Thus, the authors were able to determine that the hygrothermal stresses are directly analogous to thermal stresses.

The effects of moisture induced stress states on the fatigue behavior of the material were shown to be important by Smith and Weitsman [11]. The authors considered the topic of wet fatigue where they obtained fatigue data for dry and saturated AS4/3501-6 specimens ($[0/90_3]_s$, 8-ply]) tested in air and saturated specimens tested while immersed in water. Saturation took place in an 86°F sea water bath. S-N curves for the three different cases are shown in Figure 5. The authors attributed the fact that the saturated specimens fatigued in air had higher fatigue lives, and saturated specimens in general had reduced transverse cracking, to the relief of curing induced shrinkage provided by sorption induced swelling. The combination of water being drawn in to cracks by capillary action and cyclic mechanical loading were blamed for the fact that saturated specimens fatigued while immersed in water exhibited the lowest fatigue lives. Photomicrographs also showed that these specimens suffered more extensive delamination than the specimens tested in air.

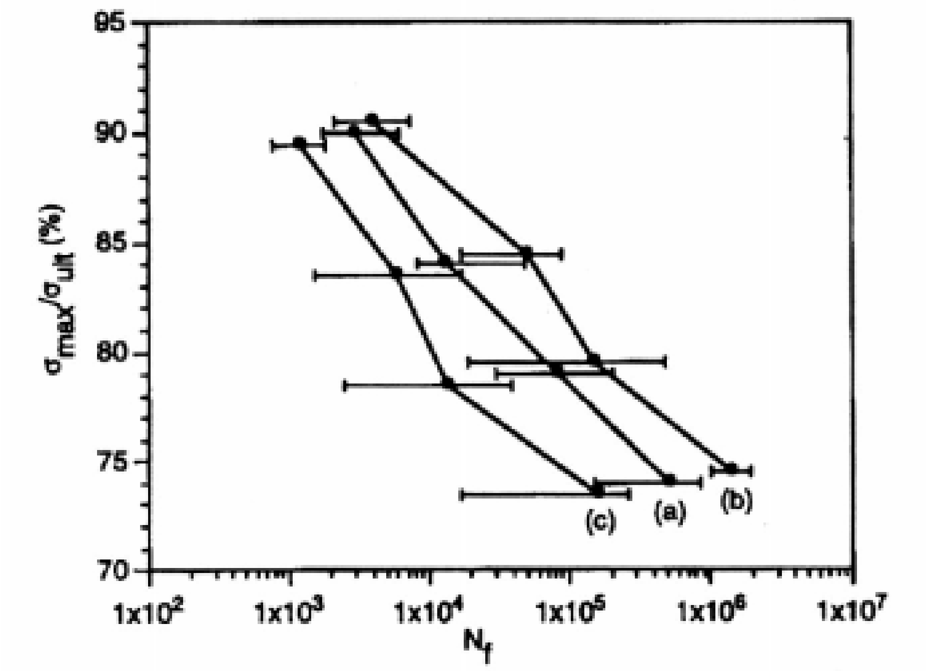

Figure 5: S-N curves for a) dry specimens fatigued in air, b) saturated specimens fatigued in dry air, and c) saturated specimens fatigued while immersed in sea water [11]

To study this behavior, the authors employed a shear lag analysis in which water trapped inside transverse cracks during immersed fatigue was included. The analysis showed that sorption and immersed fatigue affected the stress state, and the immersed fatigue in particular gave rise to cyclic tension-compression internal stresses despite the fact that the specimens were tested in tension-tension fatigue. In addition, finite elements were used to compare the delamination fracture energy for the three cases. Saturated coupons fatigued in air showed the lowest total fracture energy. The dry specimens tested in air and saturated coupons tested immersed had comparable total fracture energies but the dry specimens were predicted to exhibit mode II behavior and the immersed specimens were predicted to exhibit mode I behavior. Since the critical strain energy release rate is lower for mode I, the results correlate well with the more extensive delamination and shorter fatigue lives found in the immersed fatigue specimens. The results of this study clearly show that material intended for use in wet environments must be evaluated under continuous wet conditions in order to get a realistic idea of the effect of moisture on the material behavior.

One must also be cautious when studying hot/wet environments. Serafini and Hanson [12] considered the effects of temperature and moisture on flexural bending properties of T300 graphite fabric reinforced PMR-15 composites. They found decreasing property degradation with decreasing temperatures from T_g (approximately 316°C for this material). They also found that absorbed moisture reduces elevated temperature properties, but this effect was only evident in thermal spiking tests in which specimens were tested instantly after being placed in the heated environment. Tests conducted on specimens allowed to equilibrate at temperature showed no reduction in properties from the dry, heated case. Thus, in this case, the authors were able to conclude that the effects of moisture absorption on mechanical properties are reversible. This is an important point to consider when conducting elevated temperature/moisture studies.

Such results prompt questions about the effects of continuous absorption/desorption cycles on the mechanical properties of composites. Much of what has been done was performed in the early eighties during the push to develop the High Speed Civil Transport (HSCT). Shyprykevich and Wolter [13] presented results from a study on a notched graphite/epoxy system which was exposed to hygrothermal cycling. The hygrothermal cycle in this case was meant to simulate a tropical aircraft runway storage condition interrupted with periods of elevated temperature (261°F) representative of supersonic flights. These test results were compared with specimens exposed to a similar hygrothermal profile in which the tropical runway storage condition was replaced with a more temperate one, and the flight profile remained the same. Residual strength tests conducted at room temperature and 261°F after various intervals of exposure to both the tropical and temperate hygrothermal profiles resulted in virtually no tensile strength degradation. This result was obtained despite the fact specimens exposed to the tropical environment held an approximately 0.5% higher moisture content than those exposed to the temperate environment. However, a significant compressive strength degradation was observed. This degradation increased monotonically with moisture content up to a moisture content of approximately 1.0 percent. In addition, for the specimens with low moisture contents (0.5%), the temperature spiking encountered during cycling had no effect on residual strength. For specimens with high moisture contents (1.2%), temperature spiking did reduce the residual strength. The authors attributed this behavior to the reduction of T_g with the presence of moisture. In the low moisture content specimens, T_g was not exceeded so temperature spiking had no affect. In the high moisture content specimens, T_g of the wet material was exceeded and successive exceedences of T_g resulted in a reduced compressive residual strength.

In a related study, Whiteside et al. [14] used a nuclear reaction analysis to measure moisture distributions in specimens cycled as described by Shyprykevich et al. [13]. Figure 6 shows the results for specimens cycled under the temperate profile. One observation the authors made was that the surfaces of the specimens exhibited a 25% higher moisture content than that measured for uncycled specimens. In addition, because the central parts of the curves are all similar, the authors concluded that the moisture content at the center of each specimen is independent of the number of thermal cycles. Thus, no preferential diffusion path appears as a result of thermal spikes or microcrack formation for the material cycled under the temperate condition. Specimens that were cycled under the tropical hygrothermal condition also exhibited higher moisture contents at the surfaces than did the uncycled specimens and specimens cycled under the temperature hygrothermal condition. In addition, the moisture gradient from surface to center and center moisture content increased with increased cycling suggesting that specimens cycled longer had an enhanced moisture transport mechanism. Because SEM and DSC confirmed low microcrack density in the aged specimens, the authors attributed this behavior to deformations in the material due to the continual exceedance of T_g.

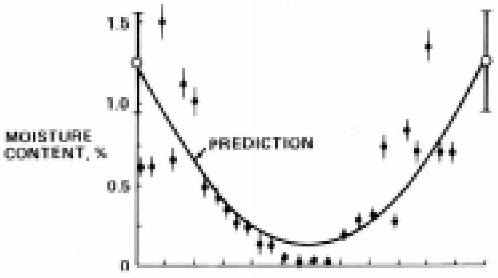

(a) 2 MONTHS

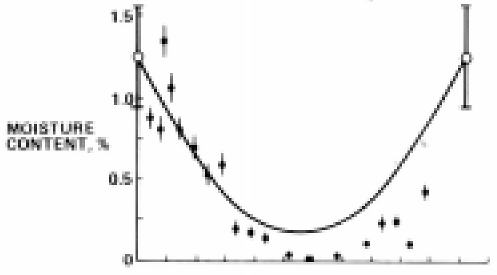

(b) 8 MONTHS

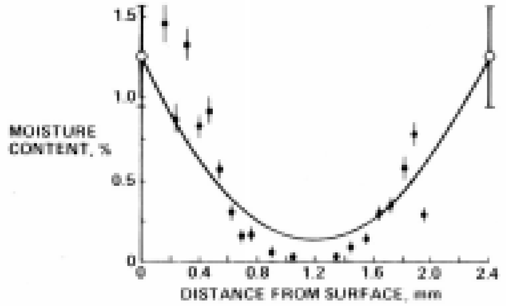

(c) 15 MONTHS

Moisture profiles after 56 days in 305 K (90°F), 70% relative humidity D_2O (temperate real-time preexposure).

Figure 6: Moisture concentration profiles of hygrothermally aged specimens [14]

In a more recent effort, Obst et al. [15] evaluated the microcracking behavior of the same AS4/PR500 five-harness satin weave being considered in the present study. Tests were conducted on “as-manufactured” specimens as well as specimens hygrothermally aged for sixteen weeks. The hygrothermal aging involved cycling the material under the temperature and moisture profile shown in Figure 1. Actual testing conditions included static and fatigue testing at room temperature and 250°F. The results of the static testing are presented in Table 1 and show that hygrothermally aged material exhibits microcracking at lower strain levels than as-manufactured material, but the final crack density at failure is minimally affected. Material tested at elevated temperature appeared to have higher initial crack strains and lower overall crack densities. This latter behavior was attributed to the relief of residual curing stresses due to the elevated temperature. Note that the modulus is unaffected by hygrothermal aging and/or elevated temperature.

Table 1: Static Test Data Obtained By Obst et al.

Material/Test Condition	Modulus (Gpa)	Microcrack Initiation Strain (με)	Microcrack Density near Failure (cracks/ply/cm)
As-mfg., RT	60.1 +/- 0.9	6000	6.1
Hygro. Cycled, RT	61.6+/- 1.5	3000	9.3
As-mfg., 93°C	60.3+/- 1.0	6900	1.9
Hygro. Cycled, 121°C	60.7+/- 0.8	4500	2.1

On the other hand, fatigue cycling at elevated temperature resulted in higher crack densities, as did hygrothermally aging the material. For as-manufactured specimens tested at room temperature, the authors found that fatigue cycling at the crack initiation strain of 6000 με resulted in more rapidly increasing crack density and a higher end value than for lower strain levels. In addition, the final crack density from fatigue cycling at 6000 με was higher (10 cracks/cm/ply) than that found from the static testing. Thus, the authors found that the nature of loading and testing environment affected the microcracking behavior of the material.

The significance of the presence of microcracking during exposure to more aggressive environments was demonstrated by interlaminar shear (ILS) test results for specimens either uncracked or cracked prior to hygrothermal cycling. The pre-cracked specimens were found to have a 25% and 15% lower ILS strength at room temperature and elevated temperature, respectively, than uncracked specimens. In addition, the presence of microcracking was found to impact the diffusion behavior of the material when exposed to 70% relative humidity at 40°C. The maximum moisture content of saturated cracked specimens was six to eight percent higher than that of uncracked specimens, and the diffusion coefficient of cracked specimens was over five times higher than that of the uncracked.

In a related study, Roy and Xu [16] have developed a moisture diffusion model that incorporates pre-existing damage conditions, such as aging induced cracking. The model is based on irreversible thermodynamics applied within the framework of continuum damage mechanics. With the use of a special form of Gibb’s potential, governing Equations are developed which are capable of modeling the effects of complex stress, temperature, damage, and moisture concentration of the diffusion process in an orthotropic material. The authors present data (from outside references) on the same five-harness satin weave used in the present study which show that the diffusivity goes up with crack density. Such data indicates that cracking does provide an enhanced transport path for moisture. Using a quadratic fit to damage (crack density) versus diffusivity data, the authors are able to establish constants needed for the analysis. The model provides very reasonable agreement with moisture uptake data. Both the model and the data show that the diffusions curves for the uncracked and cracked cases are not Fickian. Moreover, it is interesting to note that, in the data used by the authors, cracking does not influence the moisture saturation level from the uncracked case.

2.2.2 Temperature Effects

While carbon fiber properties remain generally intact from the temperature range of 68°F to 1112°F, matrix and fiber/matrix interfacial properties of PMC's may degrade significantly. Through their own studies and literature review, McLaughlin et al. [17] found that:

1) Increasing temperature may cause significant reductions in the strength and stiffness properties of epoxies. Such reductions may start to occur at temperatures well below T_g. Moreover, at high enough temperatures, the reductions may be permanent.
2) Outgassing of water vapor and organic volatiles may result in the formation of micro- and macro-cracks in the resin
3) The above phenomena are magnified with increasing time-at-temperature and moisture content.

In addition, McLaughlin et al. [17] state that the following two heat induced damage mechanisms may affect the strength and life of the composite material system:

1) Residual fiber/matrix interface damage which manifests itself as an increased initial ineffective length. Such a mechanism may reduce fatigue life even if there were no matrix property alterations.
2) Irreversible matrix property alterations. This mechanism is usually of concern at temperatures at or near T_g.

Finally, it is well known that many composites are already under the influence of internal residual stresses due to the curing process because of the differences in thermal coefficients of expansion between the fiber and the matrix. The authors hypothesize that, as heating the composite reduces the radial compressive forces the matrix imposes on the fiber/matrix interface, the stresses at the interface may become tensile and decrease the shear strength at which a crack will propagate at the interface.

In their own study on the effects of temperature on the strength and life of a graphite/epoxy system, McLaughlin et al. [17] made the following conclusions, among others:

1) While fiber/matrix interface cracking due to thermal stresses probably did not occur, loss in strength and fatigue life was attributed to matrix shear and interface degradation with temperature. The property reductions were not restricted to “extreme” temperatures.
2) While maintaining heat application for less than 5 minutes at 572°F or lower will probably not cause sufficient resin degradation to reduce residual matrix properties, maintaining composite temperatures of greater than 300°F for longer than 60 minutes does cause large reductions in strength due to matrix degradation at temperature. However, even in these cases, fatigue life was not affected for cyclic stresses below the heat-degraded static strength level.

Miyano et al. [18] considered the effects of temperature on the flexural static strength and fatigue behavior of an eight harness satin woven CFRP. Such properties can be thought of as being largely dependent of the matrix. Experimental data showed that both static and fatigue strength were affected by temperature, even at temperatures well below T_g. While the effect was more pronounced at temperatures nearer T_g, the effects were identified at lower temperatures nonetheless. Since, according to Cler [5], axial fatigue behavior of PMC's may also be dependent on matrix properties, one must be cautious in such cases, as well, even when operating well below T_g.

Case [19] studied the effects of elevated temperature on the residual strength and stiffness degradation of IM7/K3B (T_g of 473°F for K3B) notched and unnotched composites. The change in matrix properties as a result of elevated temperature (350°F) was evident from the decrease in transverse strength and stiffness properties from room temperature properties. Moreover, in the unnotched specimens, a greater reduction in residual strength was observed as a function of fatigue cycles. During fatigue, the author observed greater phase lag between applied load and material response in elevated temperature specimens than in room temperature specimens. This increase in phase lag was correlated with the greater rate of energy dissipation associated with the fact that viscoelastic materials dissipate more energy under dynamic loading as temperature approaches T_g. A final major effect of temperature observed in fatigued specimens was that, while the damage modes remained the same, the rate of progression was increased.

2.3 Modeling Initial Tensile Properties of Woven Composites

Ultimately, with any material system, one would like to use the most general information known about the material and be able to predict properties of concern. For example, one could use micromechanical models (e.g., Rule of Mixtures, Halpin-Tsai, Batdorf) along with fiber and matrix property data to get ply level predictions of strength, stiffness, Poisson's ratio, etc., for unidirectional composites. Subsequently, laminate level properties may be estimated using classical laminated plate theory.

However, the complex architecture of woven systems renders many of the angle-ply modeling techniques inapplicable. Many attempts have been made to address this issue, but most are extremely complicated or too specific. Moreover, many of the treatments of woven composites focus on plain-woven composites. Whitcomb [20] showed that the behavior of plain woven composites may not always be easily extrapolated to satin weaves. In addition, because the geometry of woven composites makes them especially appealing to analyze via finite element solutions, many have done so. These models are particularly limited since any change in geometry requires a whole new model. A review of the different modeling techniques is presented by Tan et al. [21].

Of all the models developed to date, Ishikawa and Chou [22] have formulated some of the most well known and least complicated models. The authors have presented three models to predict the elastic properties of woven fabric composites – the "mosaic model", the "fiber undulation model", and the "bridging model". The mosaic model basically treats each woven ply as an assemblage of asymmetrical cross-ply laminates. The stiffness of the laminate is then analyzed using classical laminated plate theory. In the "fiber undulation model", the authors introduce a geometrical description of the fiber undulation present in woven fabrics and again apply classical laminated plate theory to each piece of the threadwise strip. Finally, the "bridging model" was adopted to treat satin weaves, where the higher local in-plane stiffness of the straight threads surrounding the interlaced regions must be accounted for. As mentioned, all three of the models are relatively easy to apply; however, the simplicity comes with the price of generality.

N. K. Naik and Shembekar [23] have developed similar methods of analyzing elastic properties of woven laminates, but their models are much more general, allowing for such geometrical issues as open versus closed weave architectures (see Figure 7). In addition, these models are 2-D in nature, accounting for undulations in both the axial and transverse directions. In a follow-up publication, Shembekar and N.K. Naik [24] described a methodology to generate a laminate configuration from the lamina configuration given in [23].

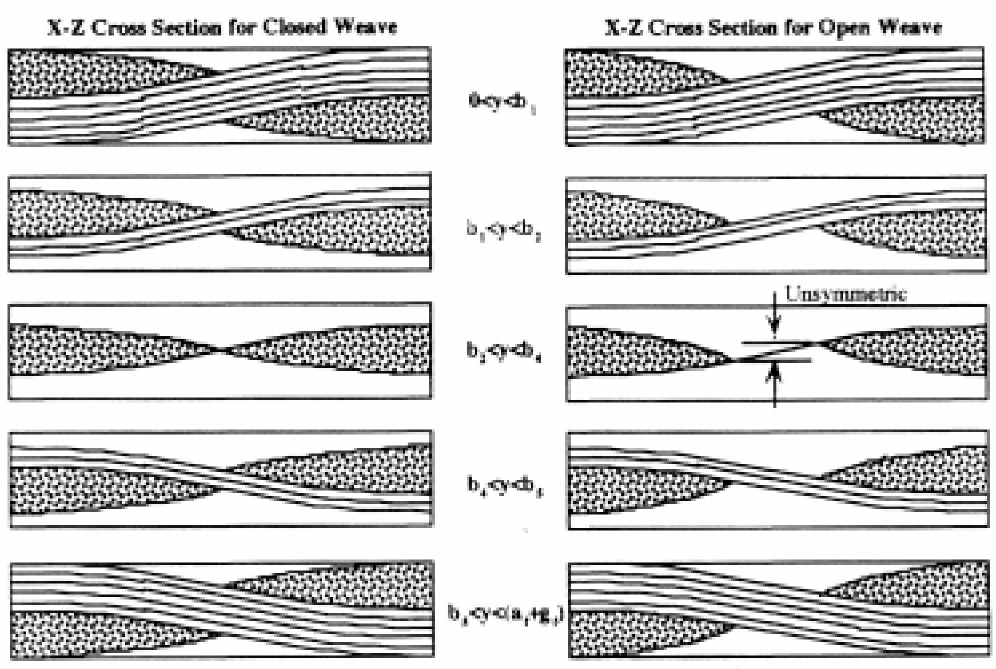

Figure 7: Closed versus open weave architecture [25]

Finally, R. Naik [26] developed a method, which was later made available as the commercial program TEXCAD, to predict strength, stiffness, and coefficient of thermal expansion of a plain woven or 2 x 2 triaxially braided composites. The method is one of the relatively few to model the strength of the woven composite. The model treats the repeating unit cell (RUC) of the composite as a spatially oriented fiber composite composed of yarn slices with transversely isotropic material properties. A volume averaging technique based on an isostrain assumption is used to calculate the overall stiffness matrix. To predict strength, an incremental approached is applied together with an appropriate failure criterion and stiffness reduction scheme. Yarn bending was also accounted for in this portion of the analysis by modeling the bending behavior of the undulating yarns as a curved beam on elastic foundation. Yarn splitting in the undulating regions was modeled as a cracked beam on elastic foundation.

All of the models discussed above provided reasonable to good agreement with data presented by the authors. After repeated attempts to obtain TEXCAD failed, the Ishikawa and Chou model was chosen for evaluation of initial stiffness in the present study because of its relative simplicity and ability to treat satin weaves. Further details on the modeling effort and the results of the evaluation are presented in Section 4.1.

2.4 Life Prediction

According to Sendeckyj [27], many of the life prediction methodologies for composites presented in the last several decades fall into one of three categories: 1) residual strength based theories, 2) stiffness degradation theories, and 3) damage mechanisms based theories. The first two are similar in that they involve the designation of a particular mechanical property as a damage metric. Failure is said to occur when the value of the damage metric degrades to a specified value. The third method involves a more complicated analysis, but may provide more accurate predictions since it directly examines the damage mechanisms which lead to failure. However, since many aspects of damage progression and accumulation are still unclear, forming a comprehensive model may prove too difficult. Talreja [28, 29, 30] has met with some success in describing the cracking behavior and delamination evolution in a cross ply laminate and has reviewed similar work in [28].

Residual strength and stiffness degradation approaches to life prediction offer the advantage of dealing with properties that are easy to measure. Residual strength approaches represent one of the most common approaches in use today, though stiffness degradation approaches hold the advantage of being given to nondestructive methods of evaluation. Stiffness-based life prediction models have been given by authors such as Pousartship and Beaumont [31], Yang et al. [32], and Whitworth [33].

Residual strength based theories are more useful when considering fiber dominated loading since residual strength is more likely to be affected in those cases than residual stiffness. Both residual strength and stiffness degradation approaches tend to come in two varieties: mechanistic or phenomenological. Phenomenological models are those which characterize strength or stiffness in terms of macroscopically observable properties, while mechanistic models quantitatively account for damage progression [34].

Some phenomenological residual strength based life prediction approaches have been given by Schaff [34] and Yang and Liu [35].

The method of choice in this study is one given by Reifsnider and co-workers [36,37], who have developed a mechanistic, non-linear life prediction model in which residual strength is assumed to be a damage metric. The model is based on the assumption that damage associated with property degradation is widely distributed within the composite and that a representative volume element (RVE) can be chosen such that the state of stress in the RVE is typical of the rest of the composite. Moreover, it is postulated that the RVE is comprised of critical and sub-critical elements, where failure of the critical element, whose state of stress is influenced by the sub-critical elements, leads to failure of the entire RVE and therefore composite. The residual strength in the critical element is calculated using a non-linear damage evolution equation. When the residual strength of the critical element equals the applied load, the composite is said to fail. This approach will be discussed in further detail in Section 4.3.

Chapter 3 Experimental Methods and Results

3.1 Material System and Preparation

The composite material used in this study consisted of PR500 epoxy (manufactured by 3M) reinforced with woven (five harness satin) AS-4 carbon fiber. This material was manufactured by DOW-UT using a resin transfer molding process. The panels themselves were stored and distributed by NASA-Glenn Research Center. Although initial plans called for the laminates to be symmetric, a burnout test revealed the layup to be asymmetric. The burnout test involved heating a composite sample to 400°C to burn off the matrix so that individual plies could be separated. This process showed that the layup of the laminate was actually {warp/weft/warp/weft/weft/warp/weft/warp}. In the first ply, the warp fibers were aligned with the 0° axis, and in the second ply, the weft fibers were aligned with the 0° axis, and so on. In this case, the weft fibers were woven through the warp fibers and are analogous to a 90° ply. Because of the nature of the weave, doubling plies of a given direction in the middle of the laminate, similarly to the process of fabricating symmetric cross-ply laminates, actually results in an asymmetric laminate.

The thickness and fiber volume fraction of each panel were nominally 0.11 inches and 55%, respectively. Panels were cut and ground by the Engineering Science and Mechanics machine shop into 8’’ long by 1’’ wide coupons. The coupons were then dried in an oven at 200°F for 24 hours and subsequently stored in a dessicator until ready for testing.

3.1.1 Moisture Saturation

Specimens that were to be tested under the humidity condition (discussed in Section 3.2) were stored in a self-made humidity chamber so they could achieve saturation. For future reference, these specimens will still be included as part of the "unaged" material group in the following sections to distinguish them from material that was aged using hygrothermal cycling. The humidity chamber consisted simply of a 927in^3 box in which was placed a beaker of a supersaturated solution of potassium chloride. This solution is known to achieve a relative humidity of 85% when heated to 85°F [38]. The chamber was kept at 85°F by placing the box in a forced air oven heated to the specified temperature. A Fisher hygrometer pen, also placed in the chamber, was used to monitor the heat and humidity. Specimens were placed on 3 shelves above beaker and were weighed prior to being placed in the chamber. Weight measurements were taken on a Mettler 200 AE balance at various intervals afterwards to track moisture uptake and assess saturation state.

3.1.2 Hygrothermally Aged Material

Hygrothermally aged material was also provided by NASA-Glenn Research Center. This material was aged for either 6000 hours or 12000 hours according the hygrothermal profile shown in Figure 1. Subsequent to the cutting and grinding process, the specimens were dried in an oven at 200°F for 24 hours.

3.2 Testing and Equipment

Since one of the main objectives of this project was to use a residual strength based approach for life prediction of the specified material, the testing program was set up to obtain residual strength data. Since relating damage state to residual strength was also of interest, several intermediate steps were taken to track damage progression. Finally, as the change in remaining strength and damage state with different environmental conditions was of particular concern, the tests on unaged specimens were conducted under each of four conditions:

1. Room temperature (72°F (22°C), to provide baseline behavior)
2. Elevated temperature (250°F, 120°C)
3. Wet (saturated and then tested at 85% relative humidity at 85°F (30°C))
4. Hygrothermal cycling (to be discussed in Section 3.2.3)

In addition, room temperature and elevated temperature tests were also conducted on material that was aged hygrothermally for 12000 hours.

For each different environmental condition, the following steps were taken to track damage progression and measure remaining strength. Each of these steps will be discussed in more detail in the sections to follow.

1. Quasi-static tests to determine initial tensile properties
2. Nondestructive evaluation to determine pre-fatigue damage state of material
3. Fatigue tests to establish S-N curves and estimate life (only for unaged material)
4. Fatigue cycling to induce damage state
5. Nondestructive evaluation to assess fatigue induced damage state of material

6. Quasi-static tests on fatigued specimens to determine residual properties

Additional quasi-static tests were performed at room temperature to determine the effect of the anti-symmetry on tensile loading behavior. These tests were conducted in both the axial and transverse directions in order to verify the balance of the weave. Finally, hysteresis loops were conducted to determine the effect of transverse tow cracking on the overall stiffness of the material.

3.2.1 Mechanical Testing Equipment

All tests were performed in load control on a MTS servohydraulic load frame. For convenience, elevated temperature, moisture, and hygrothermal testing were all conducted on a load frame different from the one used for room temperature testing. For the “environmental” testing, a Russells environmental chamber was used to control the temperature and moisture conditions of the air surrounding the specimen. Because the grips of the load frame were enclosed in this chamber, the entire specimen was exposed to the prescribed condition.

Specimens were endtabbed, 1½” (38.1mm) on each side, with a steel woven wire cloth (100 x 100 linear inch mesh with .0045 in wire diameter, obtained from McMaster Carr). Within the remaining 5 inches (127mm) of the specimen, a 1” (25.4mm) gage length MTS extensometer was used to measure axial strain. The knife edges of the extensometer were mounted on the specimen by way of v-notched aluminum tabs that were centered and bonded to the specimen using GE silicone adhesive. The extensometer was held on the specimen using rubber bands for room temperature tests and steel springs for the elevated temperature and moisture tests. The steel springs were used because the rubber bands did not hold up under the elevated temperature and moisture conditions.

In many cases, a Micromeasurements CEA-06-500UW-350 strain gage was used to measure transverse strain. When used, strain gages were bonded to the specimens just underneath one of the extensometer tabs using M-Bond 200 for room temperature and moisture specimens and M-Bond 600 for elevated temperature specimens. Additionally, the bonded gage and terminal ends of moisture specimens were coated with a protective M-Coat C sealant from Micromeasurements. The gages were connected to a wheatstone bridge circuit, and for the elevated temperature and the moisture testing, a dummy gage was inserted in the wheatstone bridge (as shown in Figure 8) to compensate for temperature. The dummy consisted of a gage bonded to an unstressed sample of material that was placed in the test chamber with the test specimen.

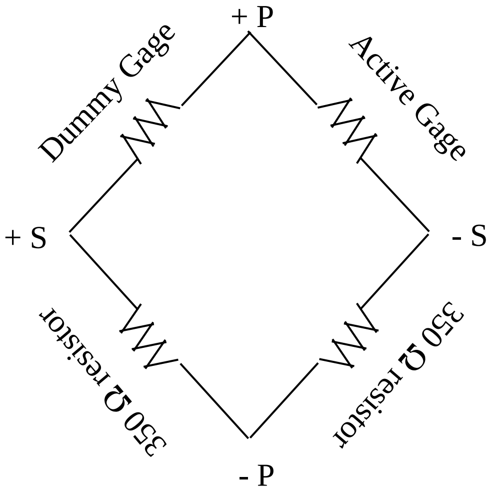

Figure 8: Schematic of the wheatstone bridge with the dummy gage

Both the extensometer and strain gage signals were run through external amplifiers. Load, stroke, and strain signals were all recorded using a computer controlled data acquisition system. For temperature and moisture testing, a (Vaisala) probe was used in the environmental chamber to monitor conditions. While the chamber came with such a sensor, the placement was relatively far from the specimen, so the additional probe and thermocouple were placed close to the specimen. The voltage signals from the probe were also recorded using the data acquisition system.

In some cases, acoustic data was also acquired. This data was obtained using a Physical Acoustics Spartan AT acoustic emission system and a broadband transducer. After low residue ultrasonic couplant was applied to the contact surface of the transducer, the transducer was secured to the test specimen with masking tape.

3.2.2 Quasi-Static Testing

Quasi-static tests were conducted in load control at a rate of 200 lbs/sec and were held in the grips of the load frame with a grip pressure of 1000 psi. Tests to determine initial tensile properties were conducted on unaged specimens at room temperature and elevated temperature and on moisture saturated specimens. A specimen hygrothermally aged for 12000 hours was also tested. Specimens that were tested at elevated temperature were allowed ten minutes to equilibrate once the chamber achieved the prescribed condition. Failure was said to occur when all or most of the plies separated. For the tests used to measure initial tensile properties, a transverse strain gage was bonded beneath the extensometer tabs to measure transverse strain. While this was also attempted for the residual strength tests, the dye penetrant used in the radiography process often inhibited bonding of the strain gage to the specimen. An attempt was made to use a ½’’ MTS extensometer to measure transverse strain, but the small strains involved required the use of high gain settings, and the resulting data contained a great deal of noise.

In obtaining hysteresis loops, specimens were loaded to increments of the ultimate tensile strength and then unloaded. After each unloading, an edge replica was taken as described in Section 3.2.4. The first load used in the process was 3500 lbs. After the next load of 5000 lbs, the load was incremented by 1000 lbs until the specimen failed. Acoustic emission data was also acquired during this process as another means of relating cracking events to stress level and testing condition.

3.2.3 Fatigue Testing

Tension-tension fatigue testing was conducted with an R-ratio of 0.1 and a frequency of 10 Hz. In establishing the S-N curves, specimens were fatigued at each prescribed temperature or moisture condition and at particular fractions of ultimate tensile strength until failure. During the “wet” fatigue testing, saturated specimens were kept from drying out not only by fatiguing them at the specified temperature and moisture condition, but also by storing them in the humidity chamber between tests. Failure was said to occur when all or most of the plies of the specimen completely separated. The S-N curves were subsequently used to estimate the number of cycles required to achieve 50% and 75% life at each stress level.

For residual strength testing, differing damage states were induced in specimens by fatiguing them at 85%, 75%, or 70% of ultimate tensile strength for either 50% or 75% of life. The testing was conducted under each of the four environmental conditions listed previously for unaged material and at room temperature and elevated temperature for material hygrothermally aged for 12000 hours.

In the case where hygrothermal cycling was imposed on specimens in conjunction with mechanical fatigue cycling, a modified version of the hygrothermal cycle shown in Figure 1 was implemented. This modified version of the hygrothermal cycle was necessary, as the time frame associated with the typical mission profile was such that the specimen would fail due to mechanical fatigue before even one full hygrothermal cycle was completed. The modified cycle was imposed as follows:

1. Fatigue specimen at 85°F and 85% RH for 144000 cycles (4 hrs)
2. Remove specimen from testing chamber and place in humidity chamber (unloaded) overnight, allowing oven and grips to cool to 85°F
3. Fatigue at 250°F for 54000 (90 minutes)
4. Remove specimen from testing chamber and again place in humidity chamber overnight, allowing the oven and grips to heat to 250°F
5. Repeat process until specimen fails

Specimens had to be taken out of the testing chamber between conditions because the size of the grips made it difficult to change conditions in a reasonably short period of time. The time of testing at each condition was somewhat arbitrarily set, but based partially on the hygrothermal cycle that was used for the aged specimens and partially on the expected fatigue life at room temperature. For the temperature portion of the cycle (and also for the isothermal elevated temperature tests), specimens were allowed 10 minutes to equilibrate at temperature.

3.2.4 Nondestructive and Thermal Analysis Testing and Equipment

Several techniques of NDE were utilized to track damage, each contributing different pieces of information. Edge replication was used primarily to study matrix cracking in the 90° tows and fiber/matrix debonding and was carried out in the following way:

1. Unpolished specimens were loaded to a constant load of 3500 lbs. Initial trials of other loads showed 3500 lbs to be sufficient to open up cracks.
2. Using a syringe, a small drop of acetone was placed on an approximately 2 inch strip of acetate tape (11340 replicating tape manufactured by Ernest F. Fullam, Inc.). Before the acetone could gel on the tape, the “wet” section of the tape was held against the edge of the specimen, usually along the gage section. Thumb pressure was applied for approximately one minute.
3. The tape was finally peeled from the specimen and sandwiched between two microscope slides. The ends of the slides were taped together to keep the replica flat.

Once in slide form, the replicas were viewed under a Nikon epiphot optical microscope with Polaroid and Nikon 35mm photographic capabilities.

Scanning electron microscopy was used to examine failure surfaces of various quasi-static specimens. Small sections (approximately 0.04 in x 1.00 mm) at the failure surfaces were cut from the specimens. Since the microscope had photographic capabilities, pictures of the micrographs could be easily taken.

Penetrant enhanced radiography was used to observe delaminations and transverse and longitudinal cracks and was conducted using a cabinet x-ray system (Hewlett Packard 43805N Faxitron Series X-ray System). Surfaces and edges of specimens intended for radiography were coated with a zinc iodide solution (60 grams of ZnI_2 mixed in 10 ml each of water, isopropyl alcohol, and Kodak Photo-Flo 200) and left to “soak” overnight. The specimens were then X-rayed at 35 kVP for one minute and the film developed.

Finally, thermal analyses such as DMA and TGA were used to determine the effect of hygrothermal aging on the glass transition and degradation temperatures of the composite. Resin degradation temperature (T_D) of aged and unaged material was determined by performing TGA on a TA Instruments Thermogravitametric Analyzer 951. Specimens were heated in platinum pans at a heating rate of 20°C/min. Nitrogen was used as the purge gas. The glass transition temperature of the composite system (T_g) was determined by performing DMA on a TA Instruments 983 system. The tests were conducted in flexure mode with thermal sweeping (2°C/min).

3.3 Testing Results

3.3.1 Moisture Saturation and Hygrothermal Aging

Moisture uptake results for both unaged and aged material (hygrothermally for 12000 hours) are shown in. The diffusion coefficient of the unaged material was calculated using

$$M = \frac{4M_m}{h}\sqrt{\frac{t}{\pi}}\sqrt{D} \tag{1}$$

and came out to be 1.98 x 10^{-9} cm^2/sec. Eq. (1) was given by Shen and Springer [39] for a material which is exposed to moisture on all six sides, where M is the moisture content of a material of thickness h at any given time t, M_m is the saturation moisture content of the material, and D is the diffusivity. The diffusivity can be solved for by finding the initial slope of the moisture uptake curve $\left(\frac{M}{M_m t}\right)$ where M is plotted as a function of the square root of time.

As of this writing, the aged material has not yet reached saturation, but the higher slope of the moisture uptake curve indicates that the aged material may have a higher diffusivity than the unaged material. Such a result is likely due to aging induced microcracks. Evidence of increased levels of microcracking in aged material over unaged material (neither of which has been subjected to mechanical loading) is given by the radiographs in Figure 10. Cracks are clearly present at the crossover points of aged material and absent from the unaged material. In addition, material aged for 6000 hours only contained transverse microcracks, but material aged for 12000 hours had both transverse and longitudinal microcracks. Moreover, a higher level of transverse cracking is evident in material aged for 12000 hours over material aged for 6000 hours, indicating a progressive damage mechanism. According to [17], the cracks may also account for the darkening of the resin that was observed in the aged material. In keeping with the trend of the cracking, the material aged for 12000 hours had darker resin than the material aged for 6000 hours, and both had darker resin than unaged material. It is important to note, however, that optical microscope images of polished cross-sections of the aged material revealed that the cracks exist predominately at the surface layers of the laminate.

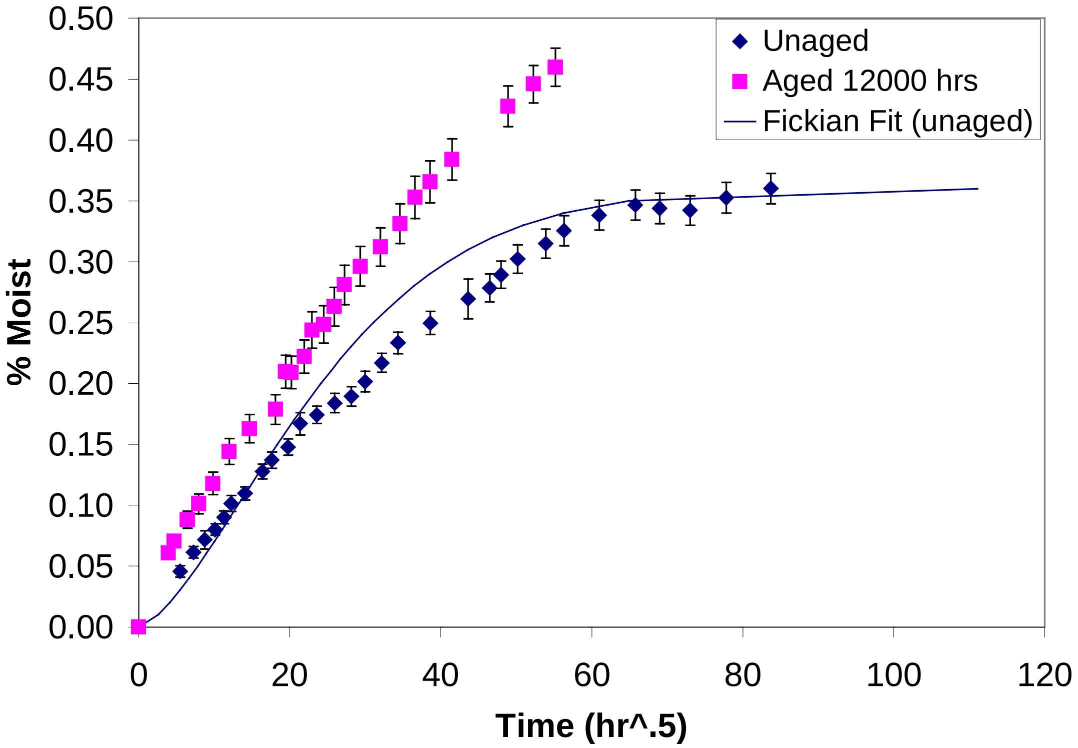

Figure 9: Moisture uptake curves for aged and unaged material

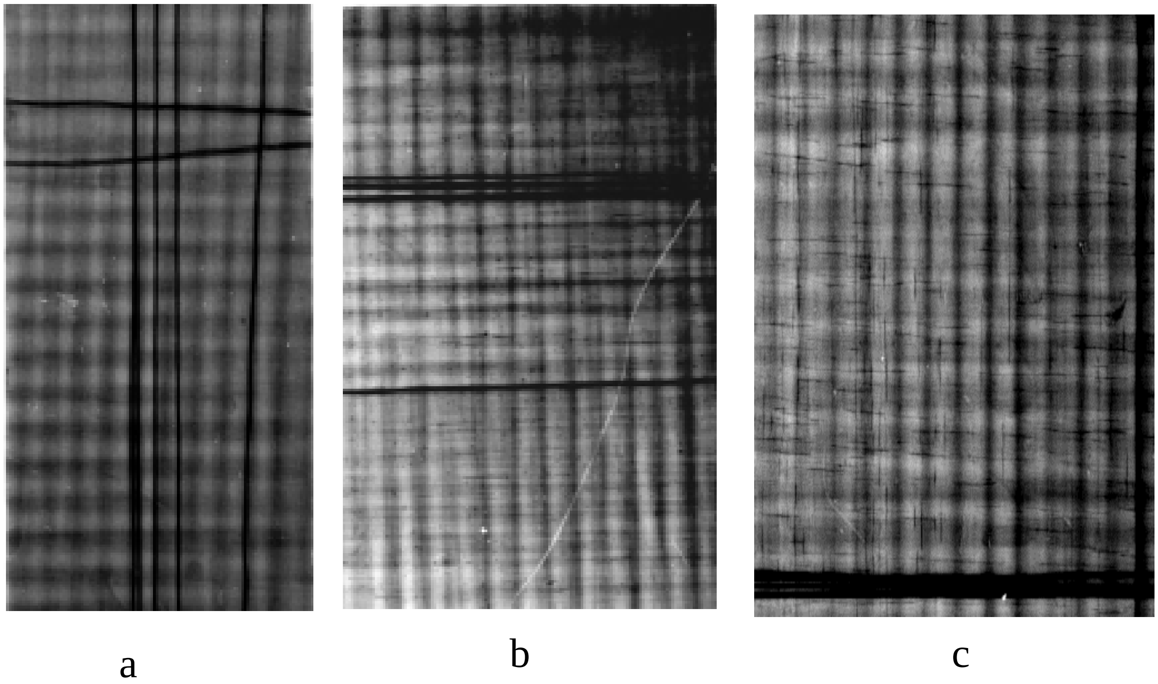

Figure 10: Radiograph of an a) unaged, b) aged hygrothermally for 6000 hours, and c) aged hygrothermally for 12000 hours specimen that has *not* been mechanically loaded

As found by Weitsman [7], moisture can be drawn into cracks by capillary action, so the cracks provide an enhanced transport system for the moisture. While this behavior may explain the higher slope of the moisture uptake curve, the higher saturation moisture content is still somewhat questionable since cracks do not necessarily hold water. As mentioned in [16], previous data on this material shows that cracks do not affect saturation moisture contents. One possible explanation explored for the higher moisture content in this case was aging induced degradation of the matrix and the consequential formation of voids. However, DMA and TGA data, found in Table 2, indicated no signs of resin degradation.

Table 2: DMA and TGA Results

Hygrothermal	T_g (°F)	Degradation Temperature (°F)
None	392	707
6000 hrs	397	747
12000 hrs	406	763

The DMA suggests that the T_g increases from 392°F for unaged material to approximately 397°F for material aged hygrothermally for 6000 hours and to 406°F for material aged hygrothermally for 12000 hours. While one may question the scatter in the data, considering the relatively small change in actual T_g, the tests were found to be repeatable. The increase in T_g is most likely due to additional crosslinking due to aging. The TGA data supports this claim, as the resin degradation temperature was found to increase significantly. In addition, the fact that polymers in general become embrittled with crosslinking may explain the microcracks in the aged material.

Another explanation for the increase in M_m that deserves further investigation is the possibility of moisture residing in the fiber/matrix interface if the interface degraded due to aging. As will be discussed later, radiographs and edge replicas indicate that the aged material did exhibit more fiber/matrix debonding during fatigue testing than did unaged specimens. This behavior supports the idea that the fiber/matrix interface may have been damaged during the aging process.

3.3.2 Quasi-Static Testing Results

The results from the initial quasi-static testing are shown in Table 3. The number in parentheses under "Condition" indicates the number of specimens tested under each condition.

Table 3: Initial Tensile Properties

Condition	Aging	Avg. Strength (ksi)	Avg. Stiffness (msi)	Avg. Poisson's Ratio
72°F (3)	None	107.9 ± 4.2	9.4 ± 0.05	0.049 ± 0.005
250°F (6)	None	100.7 ± 9.6	9.2 ± 1.0	0.038 ± 0.017
Saturated (4)	None	100.5 ± 10.0	9.4 ± 0.3	0.064
72°F (1)	12000 hrs, hygrothermal	115.6	9.0	-

Stiffness was measured by determining the slope of the stress-strain curve from 0.1% strain to 0.3% strain, as prescribed by ASTM D3039-95A for non-linear stress-strain curves. The Poisson's ratio was determined in a similar fashion with the transverse strain versus axial strain curve. Typical stress-strain and transverse strain curves are shown in Figure 11 and Figure 12, respectively. The results indicate no conclusive effect of temperature, moisture, or aging on the material tensile properties.

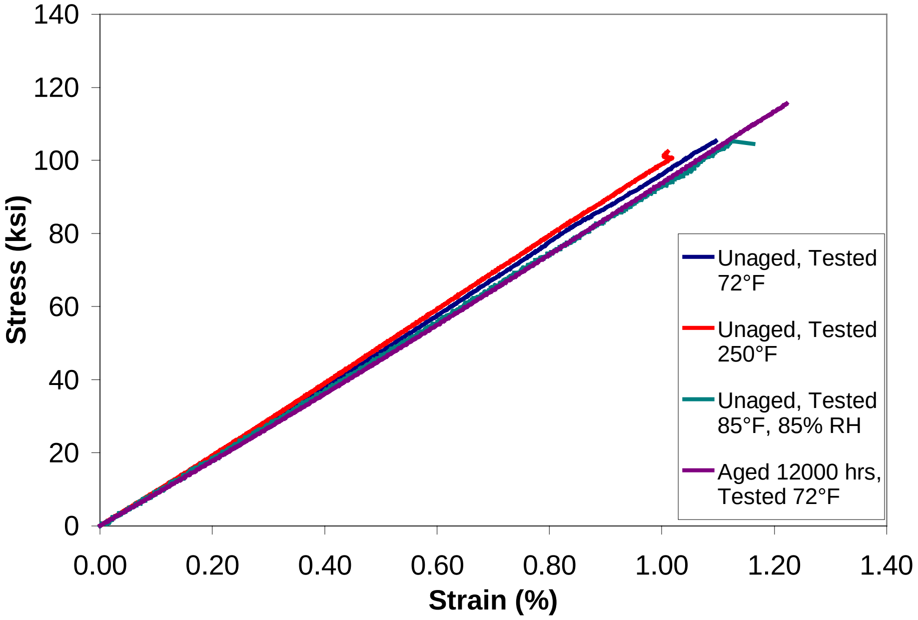

Figure 11: Initial Stress-Strain Curves

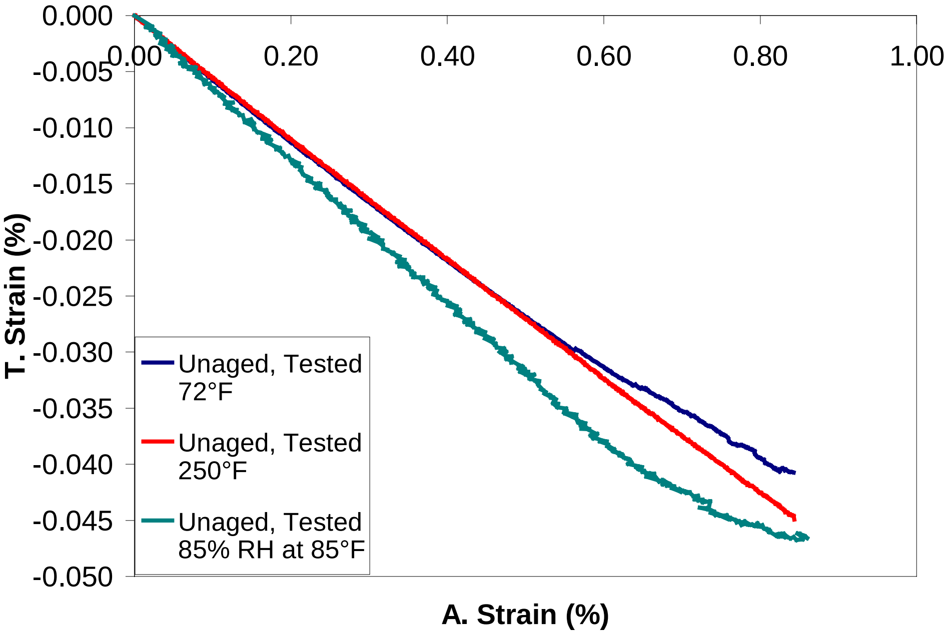

Figure 12: Initial transverse strain versus axial strain curves

Quasi-static tests were also performed on unaged specimens at room temperature to evaluate the existence of bending due to the antisymmetry of the material. The tests were conducted on specimens cut parallel and transverse to the warp direction to verify that the weave was actually balanced. Each specimen tested had both an axial and a transverse strain gage on each face. The results from such testing are shown in Table 4.

Table 4: Axial and Transverse Quasi-Static Results

	Strength (ksi)		Stiffness (msi) (Front/Back)		Axial Strain-to-Failure (%) (Front/Back)		Poisson’s Ratio (Front/Back)	
	Axial	Trans.	Axial	Trans.	Axial	Trans.	Axial	Trans.
Avg. (of 4)	100.7	109.2	9.5/ 9.2	9.8/ 9.5	1.05/ 1.06	1.08/ 1.11	0.05/ 0.04	0.05/ 0.05
Std. Div.	15.9	8.4	0.2/ 0.2	0.2/ 0.3	0.17/ 0.16	0.08/ 0.09	0.01/ 0.01	0.00/ 0.00
COV	15.8	7.7	1.9/ 2.7	2.1/ 2.8	15.99/ 14.85	7.58/ 8.29	16.65/ 15.07	9.36/ 10.57

As can be seen from the data, very little, if any, difference between front face and back face strains was encountered. This result indicates that no significant bending occurs in the material. In addition, no significant difference exists between axial and transverse properties. Thus, we may conclude that the weave is balanced and the anti-symmetry effect is negligible.

The results of the hysteresis loop tests can be found in Table 5, where 1 and 2 each refer to an unaged specimen and 3 refers to a specimen aged for 12000 hours.

Table 5: Stiffness and Crack Density Versus Load

Load (lbs)	E-1 (msi)	Crack Density-1 (cracks/in/ply)	E-2 (msi)	Crack Density-2 (cracks/in/ply)	E-3 (msi)	Crack Density-3 (cracks/in/ply)
3500	9	6.8	8.8	7.0	9.2	12.3
5000	9	6.8	8.8	8.3	9.1	17.9
6000	9	13.4	8.9	6.1	9.1	19.7
7000	9	12.5	8.9	12.3	9.2	17.9
8000	9	6.9	8.7	9.6	9.2	27.5
9000	9	16.6	8.9	8.2	9.1	23.8
10000	9	25.0	8.8	15.5	9.1	20.1
11000	9.2	28.7	8.8	12.5	9.1	27.3
12000	9.1	19.8	8.7	24.6	9.1	29.6
13000	8.8	34.1	8.7		9.0	27.1
14000	8.7				9.0	

The crack densities were quantified in the following way:

1. The slides obtained from the edge replication (as discussed in Section 3.2.4) were viewed under a light microscope at 50X. Higher magnifications revealed no further relevant details.
2. Pictures of three consecutive 2.1 mm long by 2 mm wide sections from the center of the replica (inner plies) were taken and put together to obtain a 6.3 mm long by 2 mm wide picture. A section of such a "combined" picture is shown in Figure 13. Careful examination of several replicates from specimens tested under different loading conditions revealed that such an area contained sufficient detail to characterize the quantity and regularity of cracks. However, the number of cracks along the edges of the replica appeared to be higher, in many cases, than the cracks in the center region.
3. Approximately three plies appeared in each picture. The number of cracks in each ply (note that the cracks spanned only the transverse tow of each ply) was counted and the individual totals were averaged. The average value was then divided by the length of the picture (6.3 mm) to obtain the crack density.

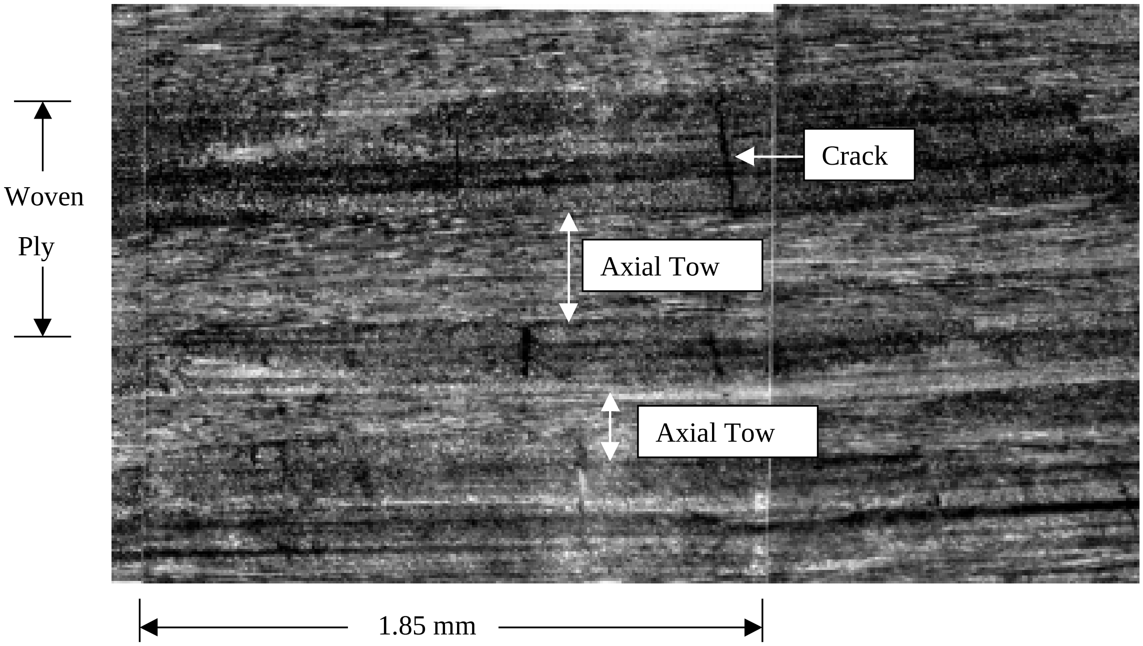

Figure 13: Edge replica section from a specimen loaded to 13000 pounds

Several observations can be made from the crack density data. First, as one would expect, the crack density increases with load. The fact that the upward trend does not appear to be monotonic can be explained by the fact that the crack densities at each load were not necessarily measured at the exact same location (though the general area was the same) of the specimen. According to [1], the CDS may be different at different crossover points. Thus, the anomalies in the crack density numbers may be due to the variability in crack density at different sections of each ply.

Another observation to be made from the crack density data is that the hygrothermally aged material exhibits higher crack densities at the lower loads. This may again be explained by the fact that the aged material contained aging induced microcracks that grew to full size early in the loading process. Interestingly, the final crack density of the material was similar to that of the unaged material suggesting that the material does reach some global CDS regardless of the aging history.

Finally, the data in Table 5 show that the stiffness does not reduce significantly (2-3%) with cracks. This behavior is further substantiated by the fact that the stress-strain curves are nearly linear elastic and do not exhibit any hysteresis, as shown in Figure 14. The fact that the curves are nearly linear is rather unusual. Typically, a knee where the stress-strain curve “bends over”, similar to the one observed for crossply materials, occurs in the stress-strain curves of woven materials. The knee generally occurs where the off-axis tows fail [22]. In this particular system, no such knee appears. One explanation that can be made for this behavior is found by examining the crack density data shown in Table 5. The data shows that significant cracking does not occur until relatively large load (stress) levels are achieved. This is further exhibited by the acoustic data shown in Figure 15. The histogram is skewed to the right, again indicating that most of the cracking activity took place at the higher loads.

Another reason for the lack of the knee may be that the axial fiber tows were actually straightening during the tensile loading process. The matrix would generally be thought to be too rigid to allow such tow straightening, but it may be possible that the transverse tow cracking relaxed the constraints on the axial fiber tows, allowing them to straighten. This straightening, and the resulting stiffening effect, may have been enough to overcome any stiffness reduction from transverse tow cracking. Such an explanation also accounts for the fact that many of the stress-strain curves actually curved slightly upwards.

However, it must be noted that many carbon fiber unidirectional specimens have been shown to exhibit similar nonlinear behavior [40].

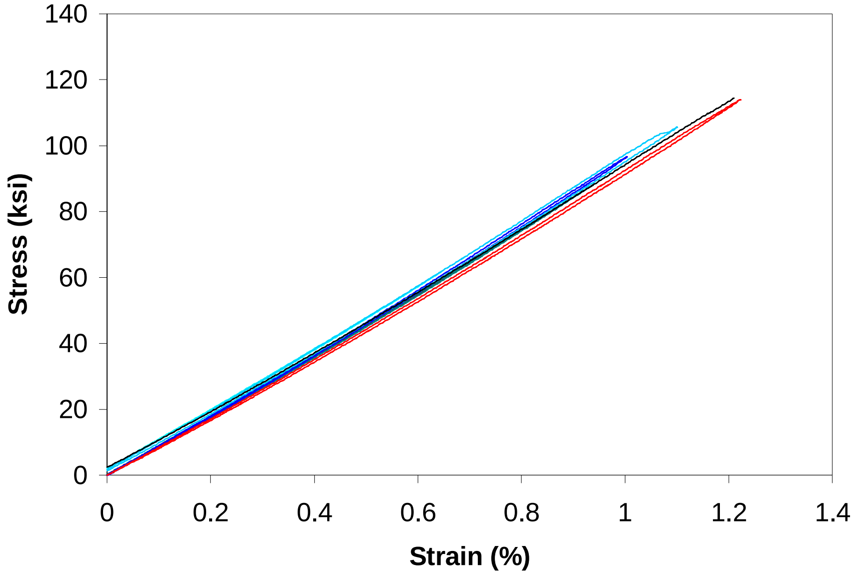

Figure 14: Hysteresis loops from a single specimen loaded to and unloaded from incremental stress levels

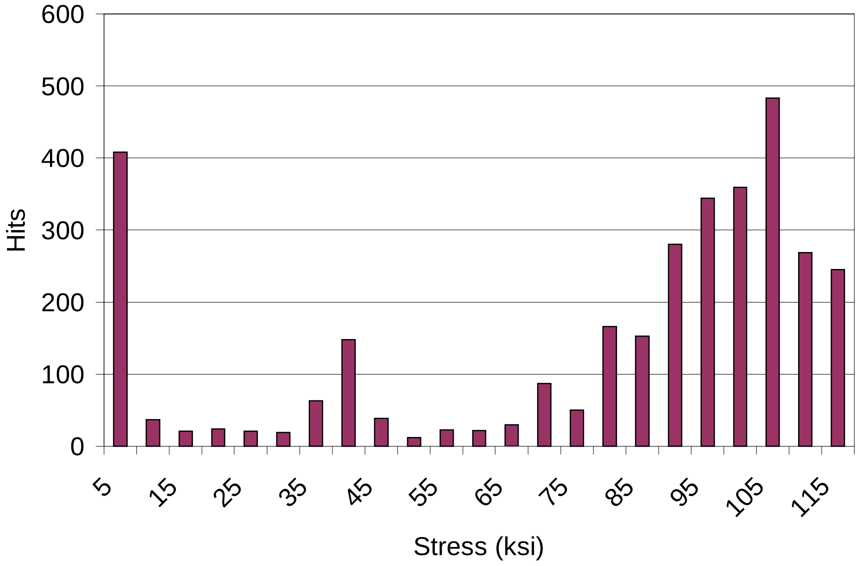

Figure 15: Acoustic emission data

3.3.3 Fatigue Testing Results

The fatigue life data for unaged material tested under each of the four environmental conditions is shown in Figure 16. The data show that only minimal differences in fatigue life occurred as a result of exposure to temperature or moisture or the combination of the two (hygrothermal cycling) during fatigue cycling. What little difference appeared manifested itself predominately at the lowest stress level (high cycle).

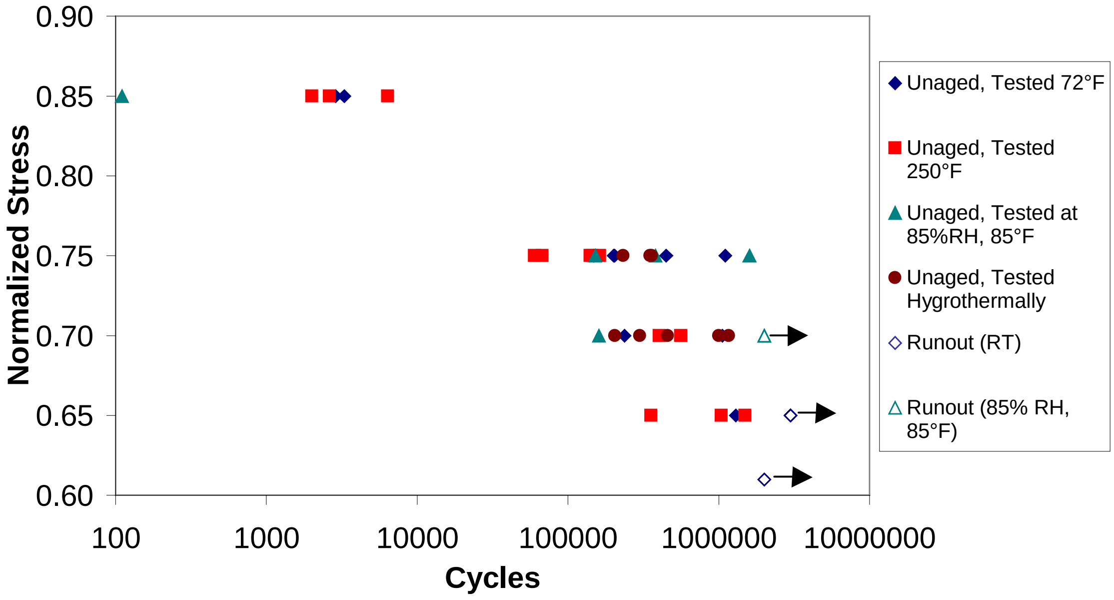

Figure 16: Maximum fatigue stress versus cycles to failure for four environmental conditions

It should be noted that some of the data points have been omitted. During the course of testing, it was noticed that specimens from a certain section of one of the panels consistently had significantly shorter fatigue lives than specimens from other parts of the panel or from other panels. The problem specimens appeared to be specimens 1-30 of the "H"-panel (panel ID provided with the laminate). Figure 17 shows the clear difference in fatigue lives between the mentioned specimens and the other specimens tested. Volume fractions measurements and SEM micrographs of virgin and failed surfaces were all examined to explain the anomaly, but to no avail. However, radiographs finally revealed a significant amount of off-axis longitudinal cracking (Figure 18) in the group of specimens in question, suggesting that these particular specimens may not have been cut exactly along the 0° axis. Another possibility may be that the fibers were moved around during the resin injection process in manufacturing.

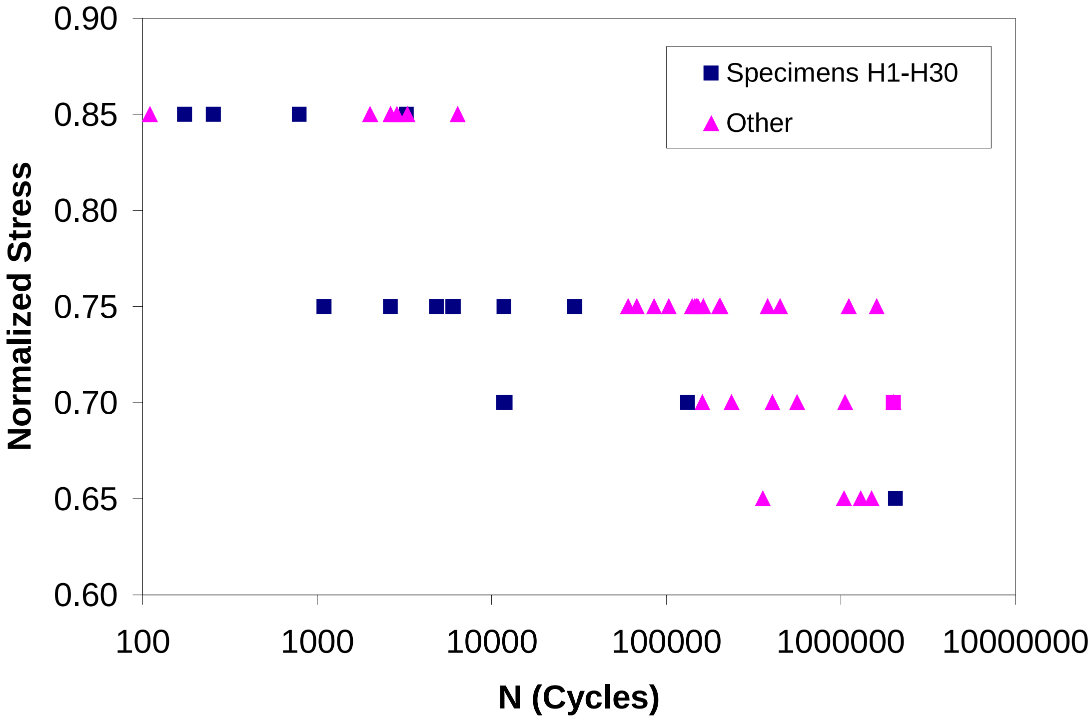

Figure 17: Maximum fatigue stress versus cycles to failure for "H" panel specimens

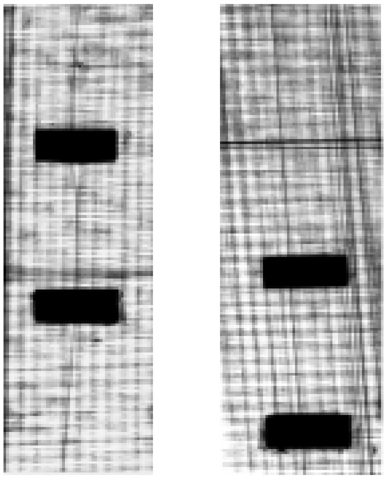

Figure 18: Radiograph of a fatigued "normal" specimen (left) and "problem" specimen (right) from the H-panel

Once obtained, the S-N data (without the "problem" specimens) were used to estimate fatigue lifetimes and fractions of lifetimes for each of the environmental conditions. Originally, average lifetimes were used to estimate the life of the material at each stress level; however, residual strength specimens fatigued according to those values tended to fail before reaching the desired number of cycles. Thus, the data was fit to a simple log-linear fit:

$$S = A + B\log(N) \tag{2}$$

where S is the maximum fatigue stress level and N is the number of cycles to failure. The results of the fits to the room temperature and elevated temperature data are shown in Figure 19 below. Note that these fits were made to S-N data which included the "problem" data points since the data was fit before the problem was realized. In addition, since many of the data points for the "wet" fatigue testing came from the "problem" specimens, the S-N curve for this condition did not show any clear trends. Consequently, the saturated residual strength specimens were fatigued according to the room temperature S-N curve.

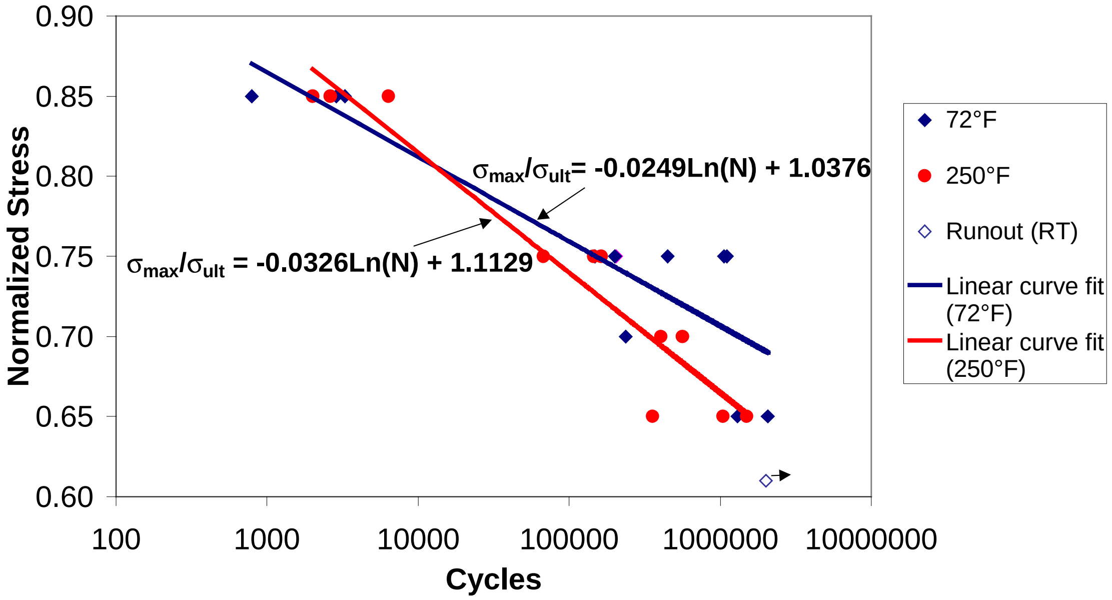

Figure 19: Unaged room temperature and elevated temperature S-N curve fits

Once the normalized (by the UTS, 108 ksi) constants to the curve fit were obtained, Eq. (2) was solved for N for normalized stress levels, S, of 85%, 75%, and 70%. The number of cycles to which the specimens were to be fatigued to achieve approximately 50% or 75% of life could then be determined. These quantities are shown in Table 6 and Table 7. The numbers of cycles to which the unaged specimens tested under the hygrothermal condition (shown in Table 8) were fatigued were chosen a little more arbitrarily, taking into account the number of hygrothermal cycles the specimens would undergo. In addition, because no S-N data was obtained for aged material, aged specimens were fatigued for the same number of cycles as their unaged counterparts.

Table 6: Estimates of life from curve fits to room temperature S-N curve

%UTS	Nf (cycles)	0.5Nf (cycles)	0.75Nf (cycles)
85	2310	1155	1733
75	170314	85157	127736
70	792370	396185	594278

Table 7: Estimates of life from curve fits to elevated temperature S-N curve

%UTS	Nf (cycles)	0.5Nf (cycles)	0.75Nf (cycles)
85	2310	1155	1733
75	170314	85157	127736
70	792370	396185	594278

Table 8: Cycles to which unaged specimens were fatigued under the hygrothermal condition

%UTS	N1 (cycles)	N2 (cycles)
75	144000 (1/2 hyg. cycle)	198000 (1 hyg. Cycle)
70	242000 (~1.3 hyg. cycles)	363000 (~2 hyg. Cycles)

3.3.4 Residual Strength Testing

Results from the residual strength testing of the unaged material are shown in Figure 20.

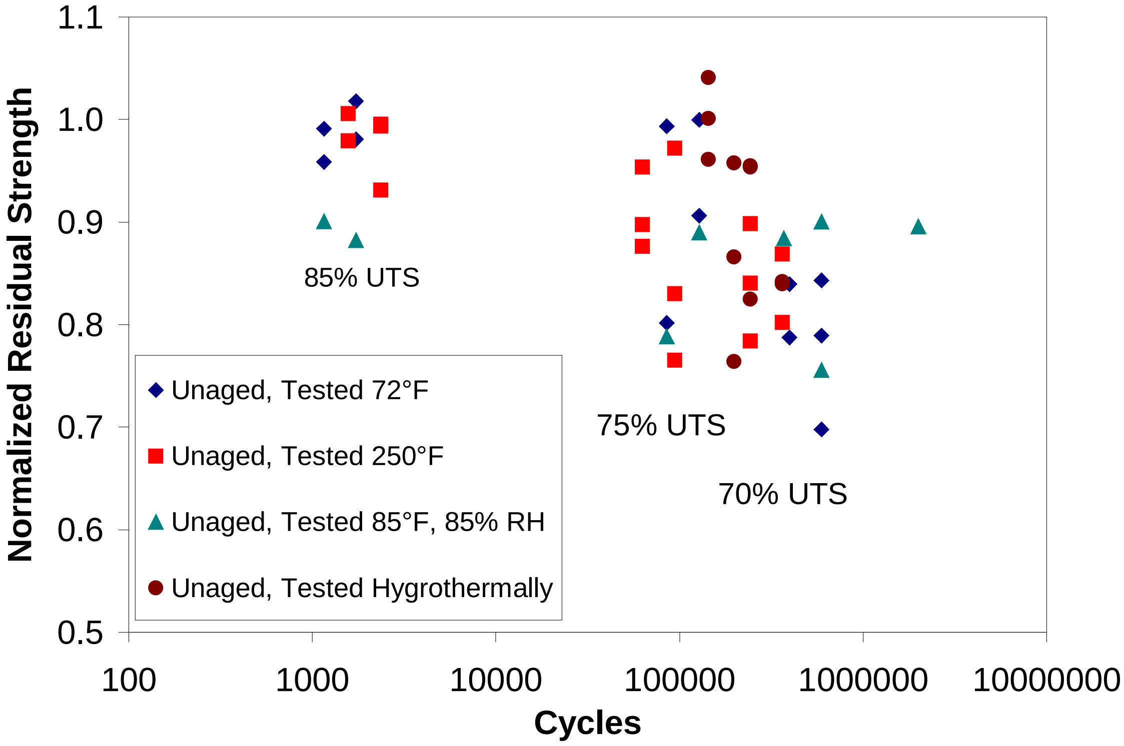

Figure 20: Unaged residual strength data as a function of fatigue cycles

The residual strengths were normalized using a strength value of 108 ksi. In every case, the intention was to get data from three specimens; however, "premature" failure of the specimens in many cases and limited material made this goal infeasible.

For the unaged material, the data shows that residual strength degrades very little, if at all, for low cycle fatigue. For high cycle fatigue, the maximum strength degradation of 20-30% occurs for specimens fatigued at the lowest fatigue stress level and for the highest number of fatigue cycles. Elevated temperature residual strength data indicate no clear departure from room temperature data. The wet residual strength data, however, is once again somewhat ambiguous. Because of the problems with the H-panel discussed in

Section 3.3.3, only one specimen tested under the moisture condition out of three survived at each stress level and fraction of life. The data that was obtained exhibits considerable scatter.

Residual strength results for material hygrothermally aged for 12000 hours and tested at room temperature and elevated temperature are shown in Figure 21. The residual strength of the aged material tested at room temperature appears to be unchanged from that of the unaged material. Some increased level of residual strength degradation is observed for aged material tested at elevated temperature, however. This was further evidenced through NDE and will be discussed in more detail in Section 3.4.

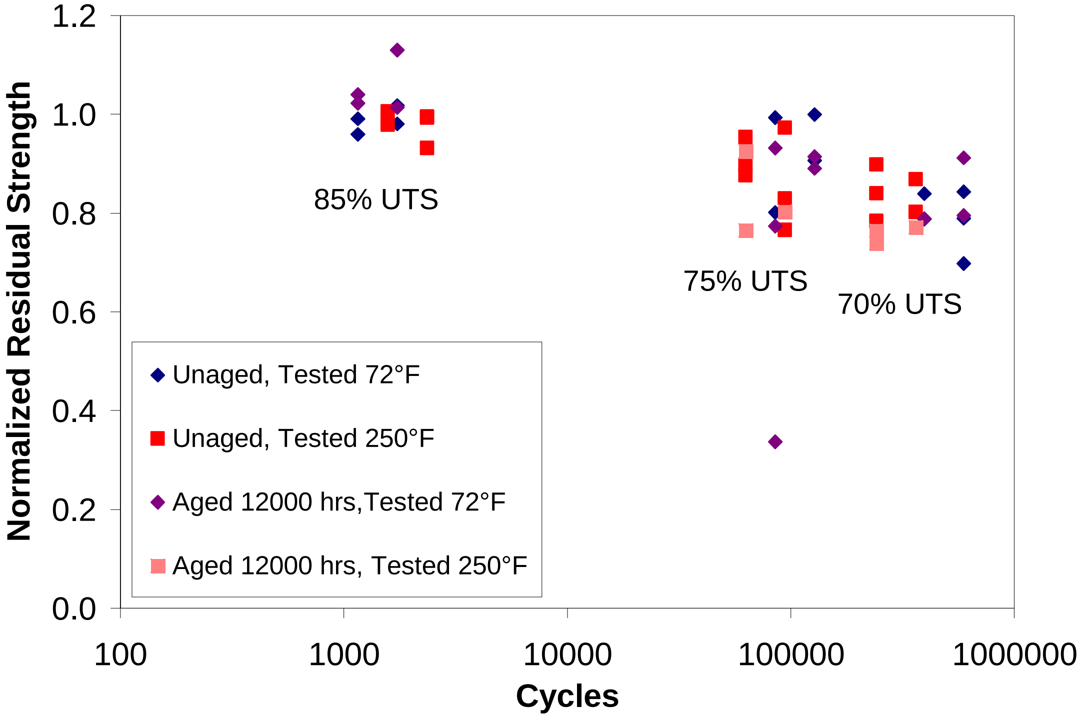

Figure 21: Aged and unaged room temperature and elevated temperature residual strength results

Residual stiffnesses were also measured for the aged and unaged material and are shown in Figure 22. In the plots, residual stiffness is normalized by 9.4 msi, the average initial stiffness. The change in residual stiffness is even less than that of the residual strength. This result may again be an artifact of tow straightening as discussed in Section 3.3.2.

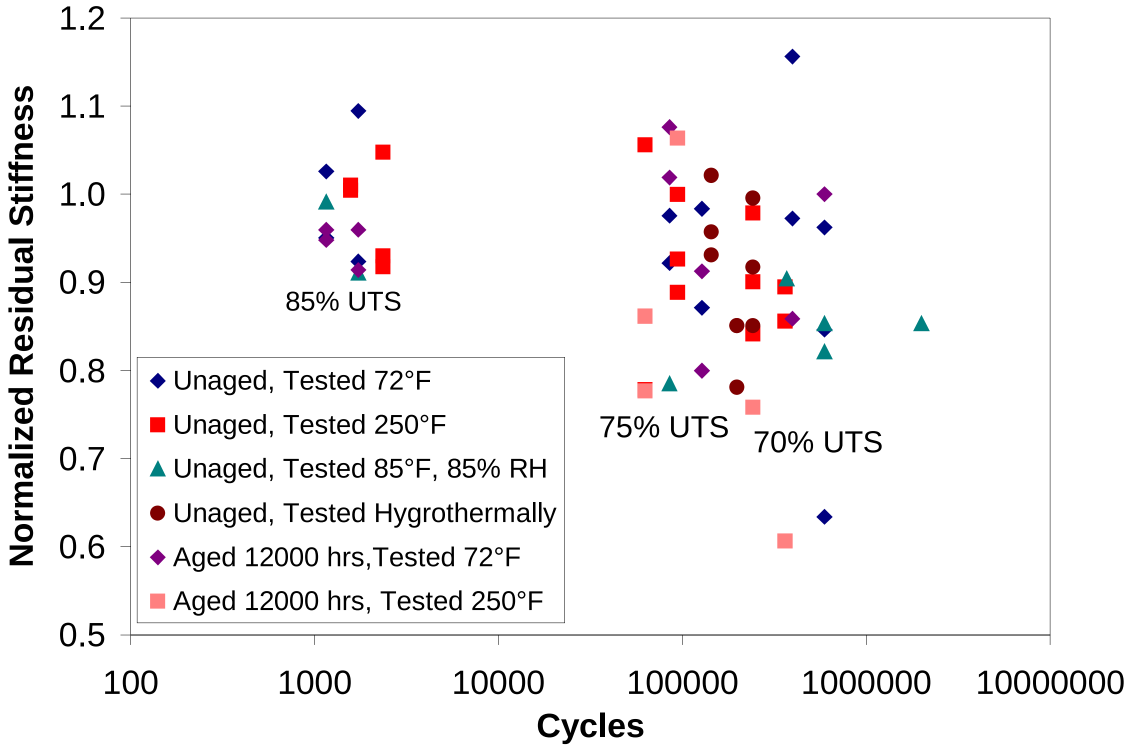

Figure 22: Aged and unaged residual stiffness results

Finally, an attempt was also made to obtain residual Poisson's ratios. However, as can be seen in Figure 23, unaged room temperature and elevated temperature data show that the Poisson's ratio measurements were inconsistent. This result is most likely due to experimental issues, and is not representative of the behavior of the material. For example, cracks appearing just under the strain gage could have influenced the data. Also, the strain gage may have been especially sensitive to the delaminations at the cross-over points. It is also worth noting that even initial Poisson's ratio data were quite scattered (see standard deviation and coefficient of variation values for initial Poisson's ratios given in Table 3 and Table 4).

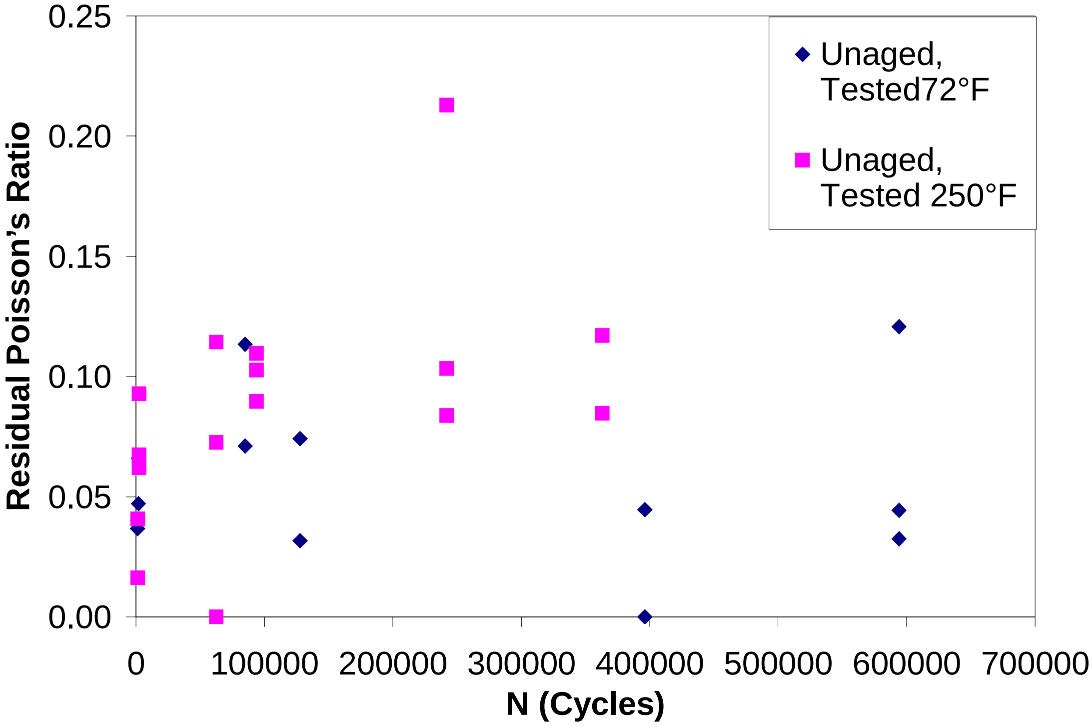

Figure 23: Residual Poisson's ratio (not normalized) as a function of fatigue cycles

3.4 Damage Progression

Radiography and edge replication were the two main methods used to follow the damage mechanisms during the fatigue process. For all unaged and aged material tested, the major initial damage mechanisms appeared in the form of transverse microcracking and delaminations at the fiber undulation areas (Figure 24). These delamination regions were also observed by Fujii et al. [1], who termed them "meta-delaminations". This initial damage was followed up with growth of transverse cracks, which extended through one transverse tow at maximum length, and the introduction of longitudinal microcracking, which did not grow significantly, around the fiber undulation areas (Figure 25). Finally, fiber/matrix debonding and edge and interply delaminations (Figure 26) typical of cross-ply laminates preceded catastrophic fiber fracture. This behavior is not unusual – it is well documented that transverse and longitudinal cracks intersecting with each other, fibers, and adjacent plies lead to delamination. The delamination inhibits the ability of the composite to distribute load, so the fibers fail as the stress increases to a critical level [3,41].

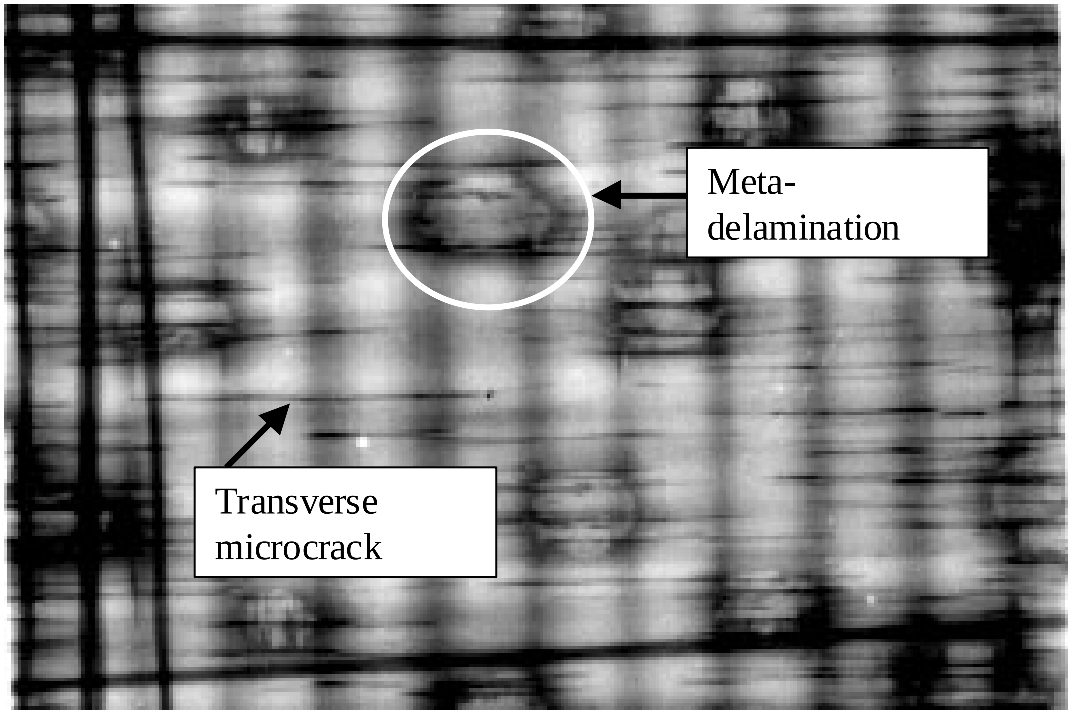

Figure 24: Radiograph of elevated temperature specimen (unaged) fatigued for 2358 cycles at 91.8 ksi (85% UTS)

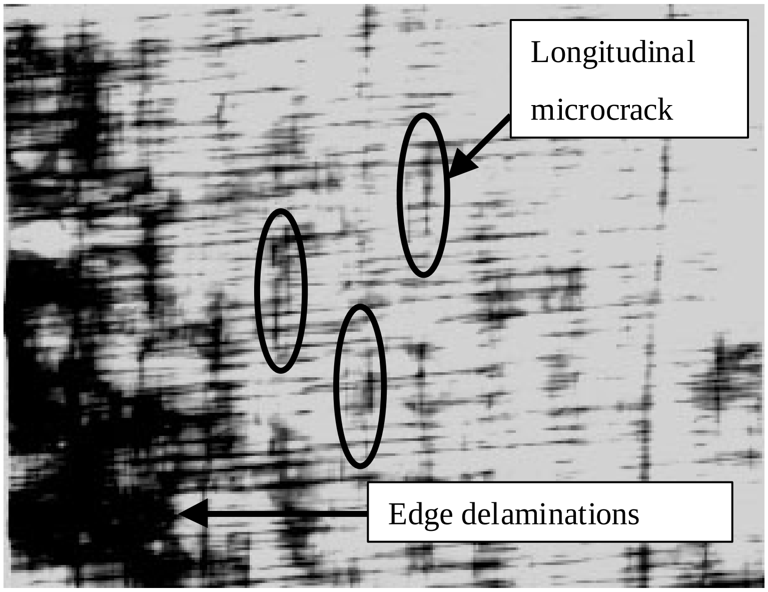

Figure 25: Radiograph of elevated temperature specimen (unaged) fatigued for 62700 cycles at 80.0 ksi (75% UTS)

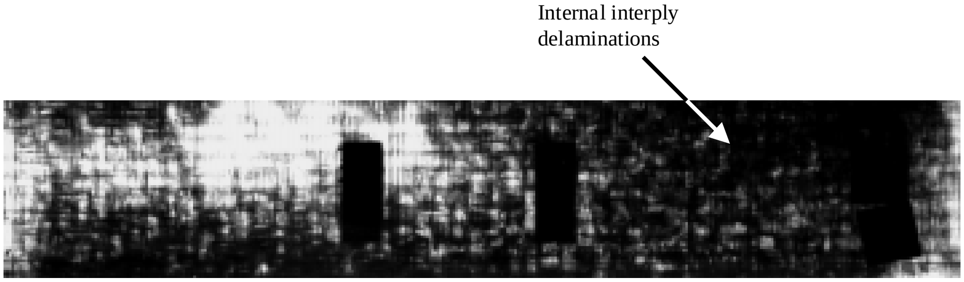

Figure 26: Radiograph of elevated temperature specimen (unaged) fatigued for 242000 cycles at 75.6 ksi (70% UTS)

One damage mechanism unique to the woven material is microcracking at the warp/weft tow cross-over points, evident in both quasi-static specimens (transverse cracking only) and fatigue specimens (transverse and longitudinal cracking). These microcracks indicate that the stresses are relatively high at the cross-over points. In fatigue specimens, these microcracks cause the fibers crossing over and under the resin rich area between them to debond fairly early in the fatigue process. Another phenomenon that appeared during high cycle fatigue that was also localized at the cross-over points was “flaking” of the resin. This was particularly true in surface tows which had clearly become debonded. An example of a fatigued specimen in which this behavior was observed is shown in Figure 27.

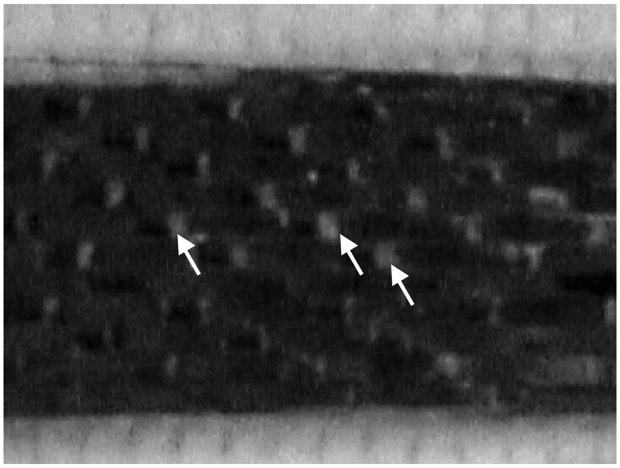

Figure 27: Flaking of resin on the surface of a specimen fatigued to failure at 70%UTS

The extent to which these damage events occurred, and the rate at which they occurred, did vary with testing conditions and fatigue stress levels. For example, an edge replica and a radiograph of a typical unaged specimen fatigued at elevated temperature at 85% UTS are shown in Figure 28. In this case, only the transverse cracking and meta-delaminations are readily apparent. In addition, the fracture surface is clean and cohesive, similar to that found in a quasi-static failure, as shown in Figure 29.

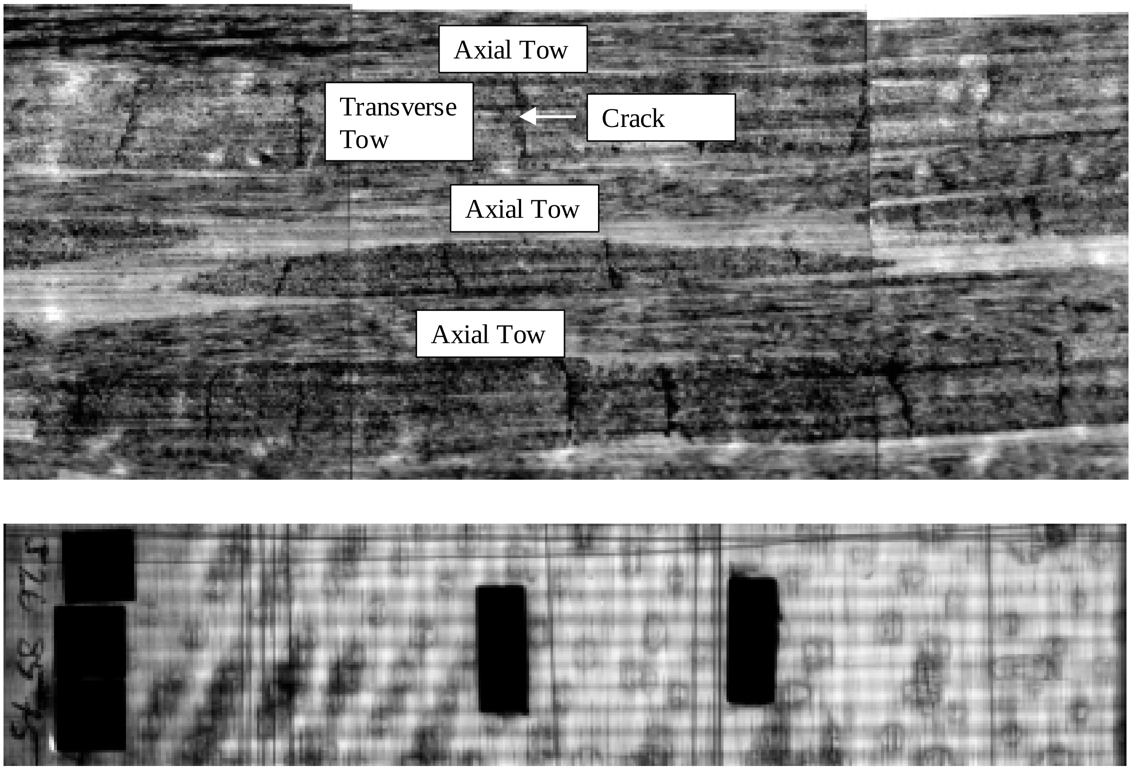

Figure 28: Edge replica (top) and radiograph (bottom) for an unaged specimen fatigued at elevated temperature at 91.8 ksi (85% UTS) for 2358 cycles)

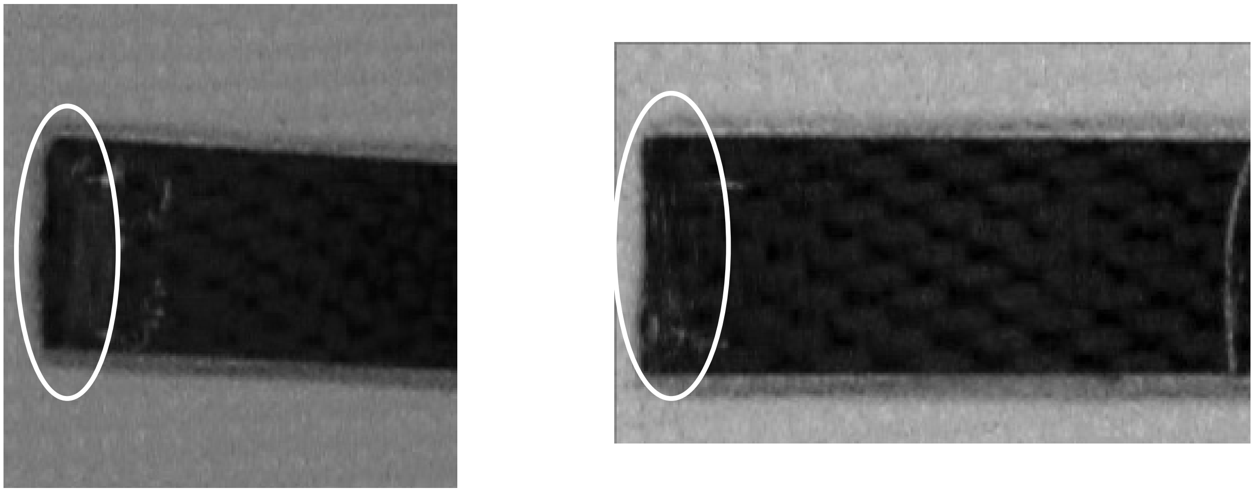

Figure 29: Failure fracture surface of a room temperature quasi-static specimen (left) and an elevated temperature specimen cycled at 85% UTS (right).

On the other hand, for a typical specimen fatigued at elevated temperature at 70% UTS (Figure 30), we see a far greater amount of fiber/matrix debonding and interply delamination. The fracture surface, shown in Figure 31, is far less cohesive than was found for the high fatigue stress level specimens. In many cases, the specimens did not completely separate into two parts. Instead, enough plies pulled apart within the composite to constitute failure, but the few intact plies still held together. This was true even in many of the residual strength tests in which the specimen strength was relatively low.

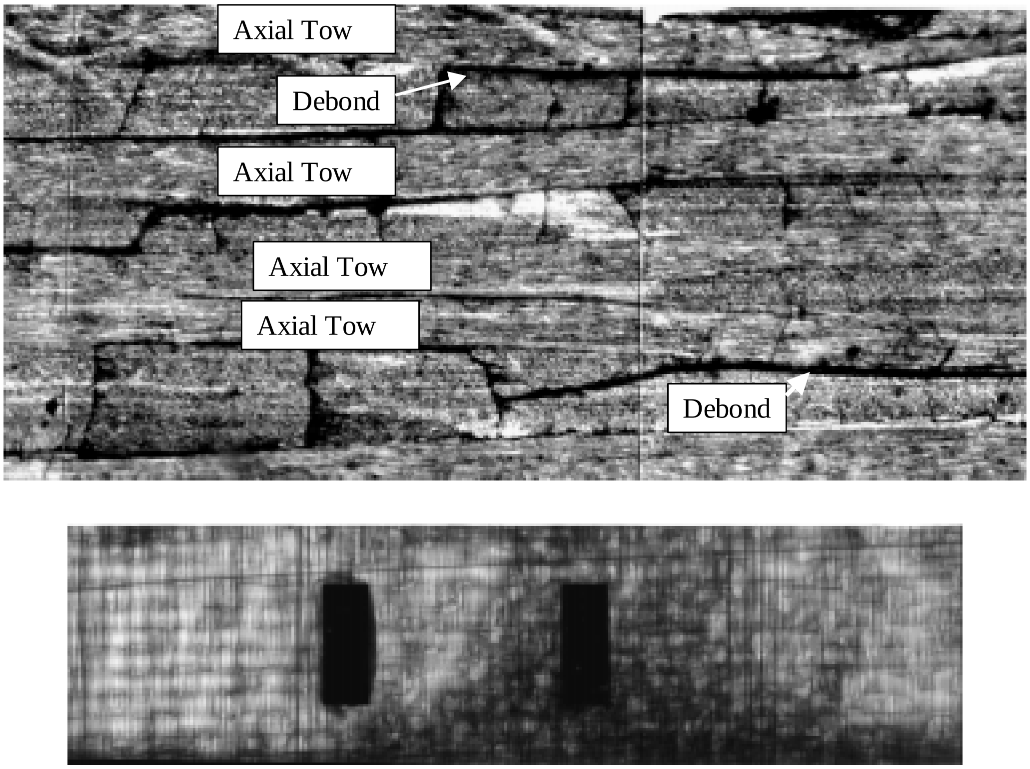

Figure 30: Edge replica (top) and radiograph (bottom) for an unaged specimen fatigued at elevated temperature at 75.6 ksi (70% UTS) for 242000 cycles

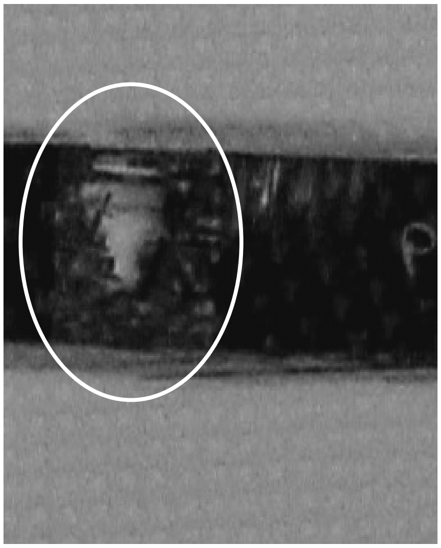

Figure 31: Failure fracture surface of an elevated temperature specimen fatigued at 70%UTS.

3.4.1 Dynamic Stiffness Loss and Damage Accumulation

The increased level of damage accumulated in the composite with decreasing fatigue stress level is manifested in the dynamic stiffness loss curves acquired during fatigue testing (Figure 32). Note that the stiffness loss follows the classic “S-shape” discussed in [3] for both the aged and unaged material. During the course of the fatigue tests, dynamic stiffness was monitored by way of the extensometer and stroke data. In many cases, the extensometer data drifted a great deal, possibly as a result of the damage progressing within the composite and particularly in the surface ply on which the extensometer was mounted. Thus, the stroke data was used to track dynamic stiffness loss and shows that specimens fatigued at lower fatigue stress levels underwent greater stiffness loss due to the increased accumulation of damage.

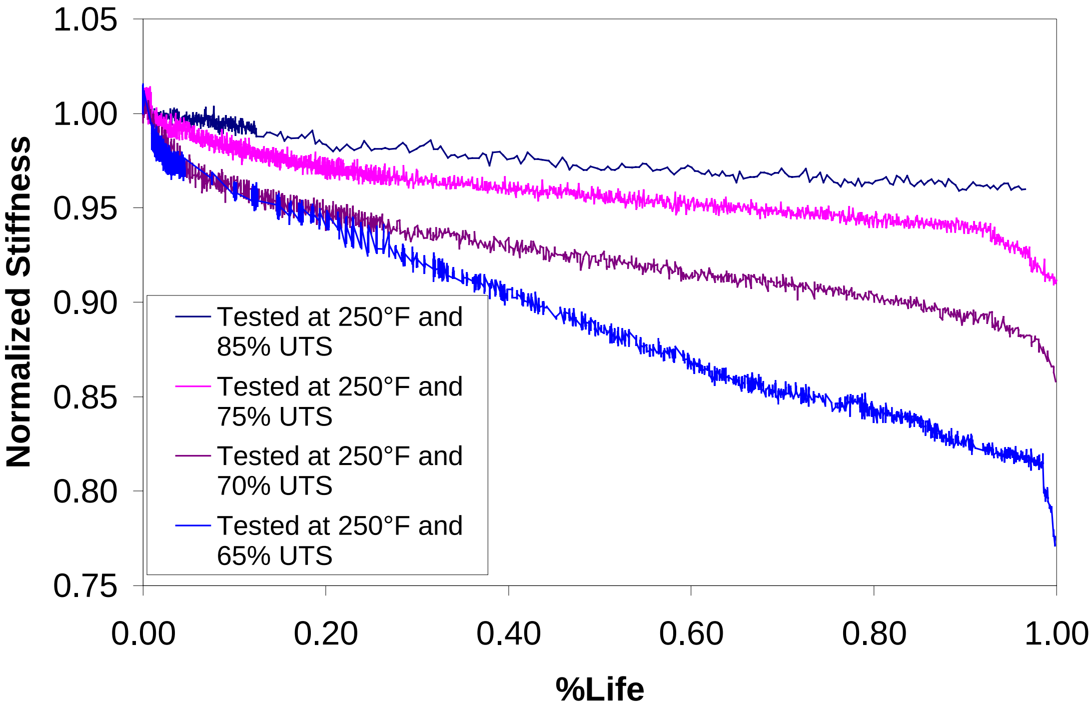

Figure 32: *Dynamic* stiffness loss curves (from stroke data) for unaged specimens tested at elevated temperature

The results are in line with residual strength and damage tolerance ideas. Considering the philosophy that fatigue failure of a specimen will occur when its remaining strength degrades to the value of the applied load, it follows that a specimen fatigued at a lower stress level must undergo more damage because the strength must degrade more. The increased level of damage corresponds to a greater stiffness loss.

Differences in the rate and extent of damage accumulation were also observed for the different environmental conditions. Figure 33 compares unaged room temperature and elevated temperature dynamic stiffness loss curves. The fact that the stiffness loss is slightly greater for elevated temperature than for room temperature indicates that specimens tested at elevated temperature suffered a greater extent of damage than room temperature specimens.

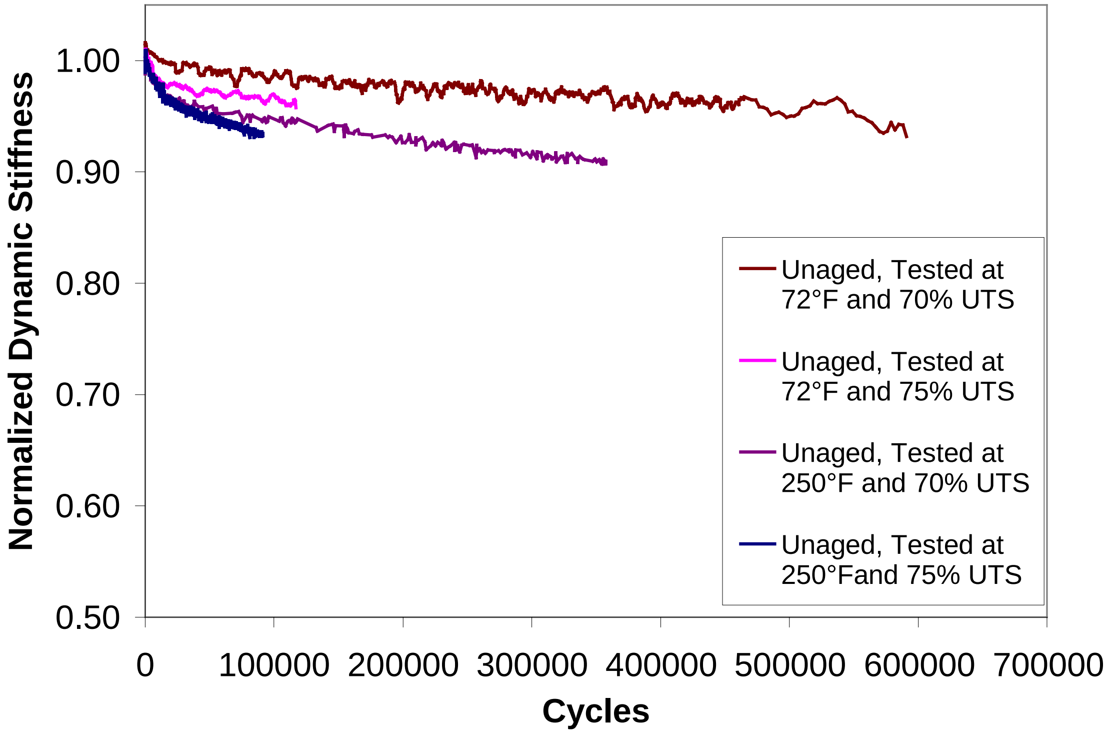

Figure 33: Comparison of room temperature and elevated temperature *dynamic* stiffness loss curves

Radiographs such as shown in Figure 35 verify that the elevated temperature specimens delaminated more than room temperature specimens. Edge replicas also indicate a greater amount of fiber/matrix debonding in the elevated temperature specimens, but edge replicas should be considered with caution since they show only a small section of the specimens. From SEM images of quasi-static fracture surfaces (Figure 34), however, it is readily apparent that the fibers in the elevated temperature specimen are debonded cleanly from the resin while the fibers in the room temperature specimen are still well bonded to the resin. This apparent increase in delaminations and fiber/matrix debonding in the elevated temperature specimens does support the ideas of McLaughlin et al. [17]. As stated in Section 2.2.2, these authors believe that heating the composite may cause the curing induced compressive stresses at the fiber/matrix interface to actually become tensile and decrease the shear strength at which a crack will propagate at the interface. The increased capacity for longitudinal debonding also increases the probability of delamination since the points where transverse and longitudinal cracks cross are in a three-dimensional stress-state and are thus common sites for delamination initiation [41].

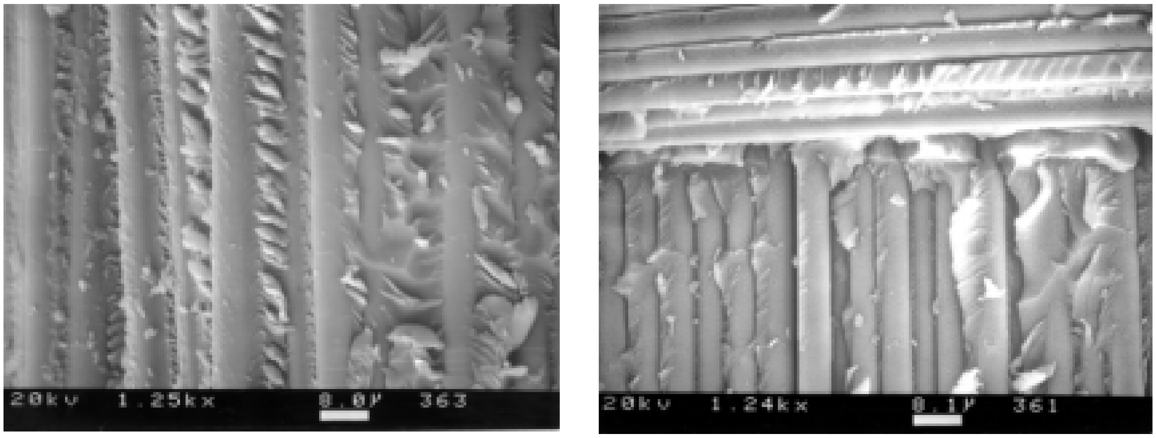

Figure 34: SEM micrographs of quasi-static fracture surfaces for unaged room temperature (left) and elevated (right) specimens

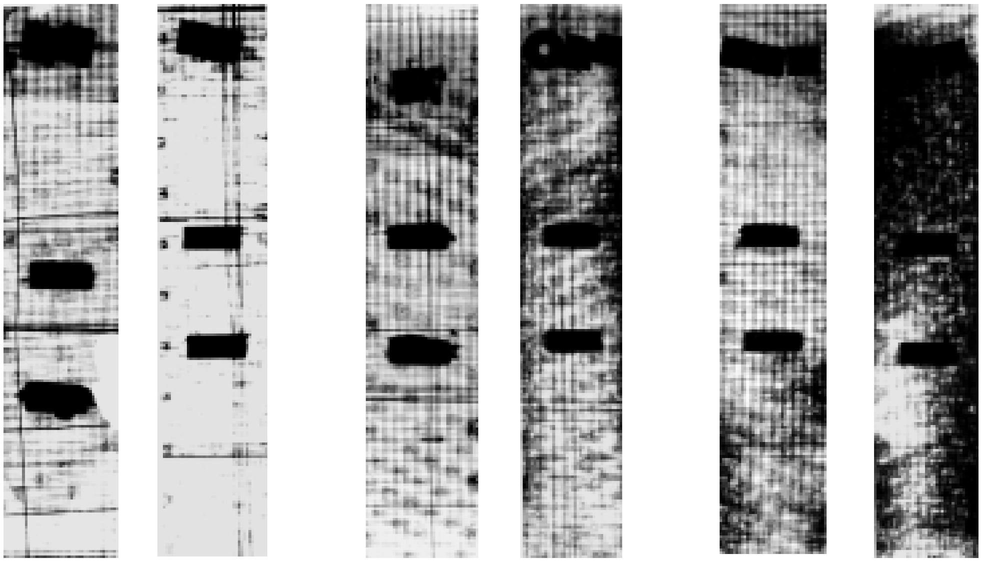

72°F, 1733 cycles

250°F, 2358 cycles

72°F, 127736 cycles

250°F, 84050 cycles

72°F, 594278 cycles

250°F, 363000 cycles

Figure 35: Radiographs of unaged specimens fatigued at room temperature and elevated temperature

Typical moisture stiffness loss curves could not be determined as the curves obtained were all too different, even for specimens tested at the same stress level for approximately the same number of cycles. In addition, only one radiograph was taken out of concern for the effects the penetrant and radiation would have on the moisture content of the specimens (and because so many of the specimens failed). Thus, most of the damage was evaluated from edge replications. Just as with the elevated temperature case, the saturated specimens seemed to exhibit a greater amount of fiber/matrix debonding than did room temperature specimens, suggesting that the fiber/matrix interface may have been degraded. To further explore this idea, fracture surfaces of saturated specimens loaded quasi-statically were observed with SEM. Figure 36 shows that the fibers at the quasi-static fracture surface of the moisture saturated specimen are indeed barer than those of the room temperature (unsaturated) specimen (see Figure 34), supporting the idea of interfacial degradation in saturated material.

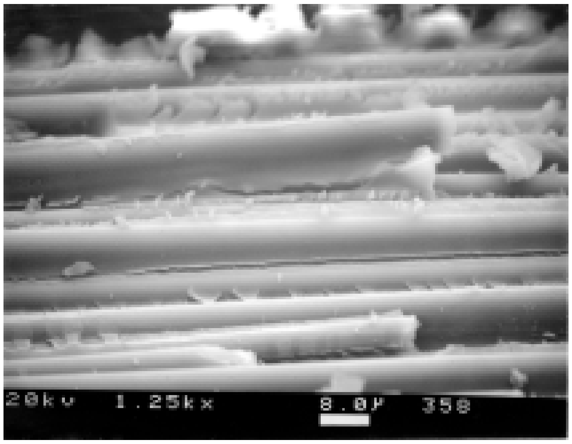

Figure 36: SEM micrograph of a quasi-static fracture surface of a moisture saturated specimen

Stiffness loss curves of unaged specimens tested in conjunction with hygrothermal cycling were also difficult of evaluate. Each time the test was stopped to change conditions resulted in a discontinuity in the stiffness loss curve. However, edge replicas and radiographs showed no real departure in damage accumulation processes from that found in unaged room temperature fatigue specimens.

Finally, as shown previously, the aged specimens started with some level of damage, in the form of microcracking, at the cross-over points. Also, quasi-static testing showed that these transverse microcracks grew to bundle length fairly quickly under loading, especially in the surface plies. Thus, we may postulate that the delamination process started earlier in the aged specimens than in unaged specimens. In any case, edge replication, dynamic stiffness loss curves (Figure 37), and radiography (Figure 38) made it quite clear that the aged material sustained much more fatigue damage than did unaged material. This was particularly true of aged specimens tested at elevated temperature. As with the moisture saturated specimens, we may again speculate that this behavior is due to some form of fiber/matrix interfacial degradation due to aging, making the effect of elevated temperature seen with unaged specimens more pronounced in the aged specimens. The quasi-static fracture surface of an aged specimen, shown in Figure 39, exhibits more fiber pullout than does that of an unaged specimen (Figure 29), also supporting the idea of interfacial degradation. Finally, the flaking of the resin at the cross-over points that appeared to occur in the unaged specimens was also apparent in the aged material. In this case, it was more obvious that the flaking was occurring in the resin because of the change in resin color.

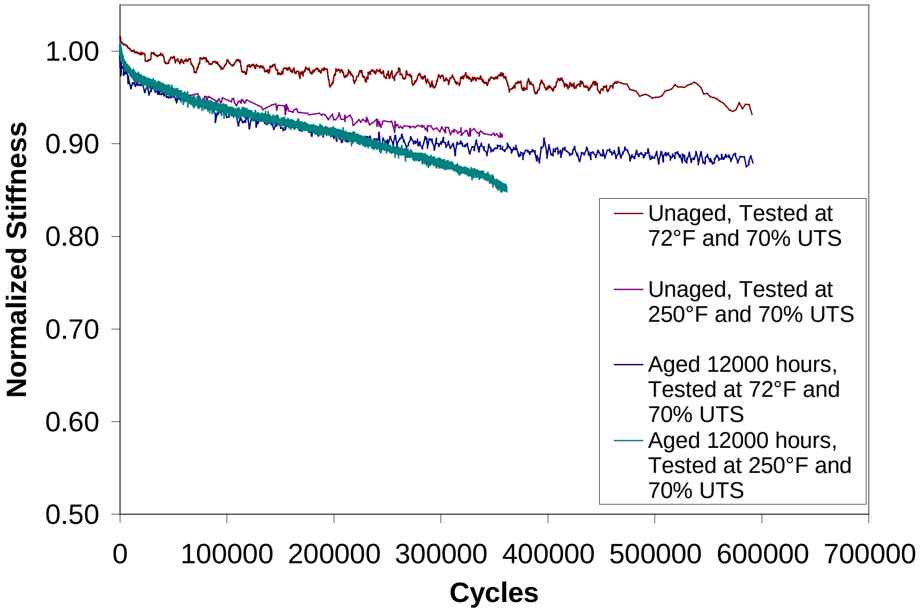

Figure 37: Dynamic stiffness loss curves for aged and unaged fatigue specimens

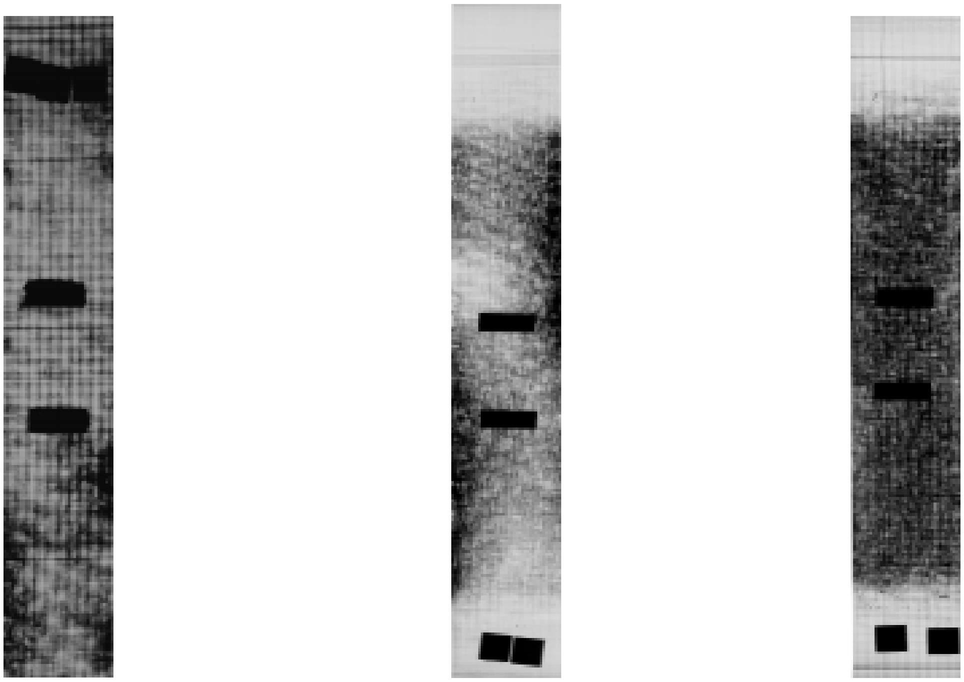

Unaged, tested at 72°F for 594278 cycles

Aged 12000 hrs, tested at 72°F for 594278 cycles

Aged 12000 hrs, tested at 250°F for 363000 cycles

Figure 38: Comparison of interply delamination for aged and unaged fatigue specimens

Figure 39: Quasi-static fracture surface of a specimen aged for 12000 hours

3.4.2 Crack Density

Transverse cracking was monitored as a function of fatigue cycles. From unaged specimen fatigue results, shown in Figure 40, it can be observed that crack density does increase as a function of cycles for much of the material lifetime. This increase occurs with increasing fatigue cycles, regardless of stress level.

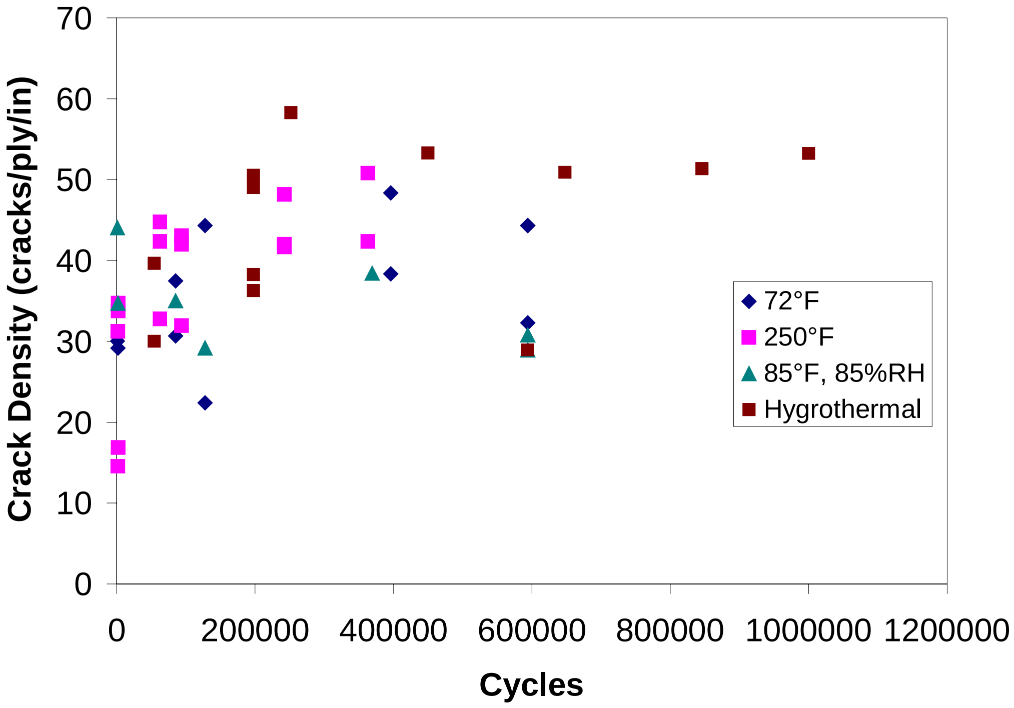

Figure 40: Unaged specimen crack densities as a function of fatigue cycles.

The data also shows that crack density remains approximately the same for all of the environmental conditions. One observation that can be made from this result, then, is that the difference in the dynamic stiffness loss between unaged specimens tested at room temperature and elevated temperature is mostly due to delamination. This is not surprising since very little stiffness loss was observed to occur with cracking in the quasi-static testing (Table 5). Moreover, O'Brien [42] linked stiffness reduction with delamination development in 1982.

The moisture saturated specimens exhibit a slightly lower crack density than specimens tested at other conditions, but more data is needed before such a conclusion can be drawn (again, "problem" specimens resulted in a lack of data). However, if the lower crack density is a real phenomenon, the idea that the moisture saturated specimens have undergone some interfacial degradation would be supported. The degradation of the interface would inhibit stress from being transferred from the debonded fiber to the matrix. As shown in Figure 41, the ineffective length around a fiber fracture would then be very large and the adjacent matrix would not be subject to the stress concentration it would normally face in a well bonded system. Thus, the matrix is less likely to see a high enough load to crack.

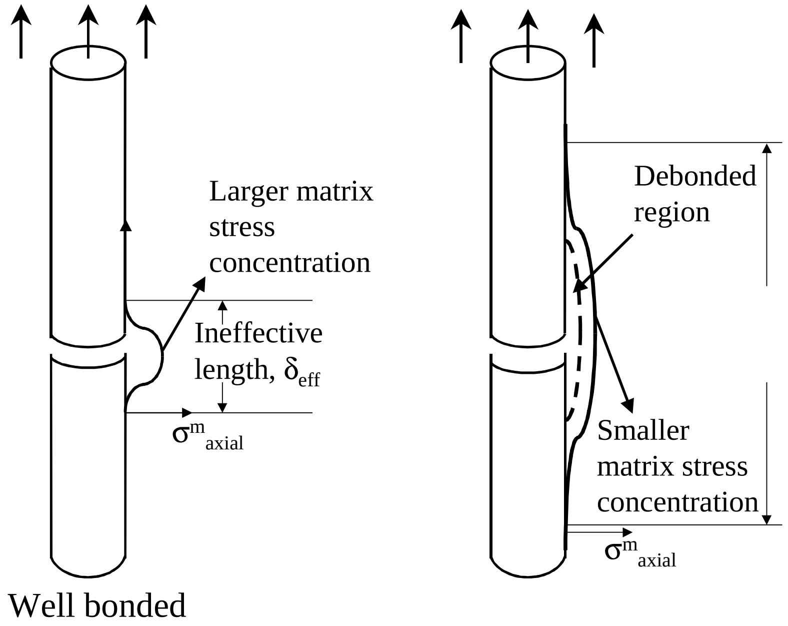

Figure 41: Illustration of the effect of debonding on ineffective length and matrix stresses

The crack saturation density of specimens tested at elevated temperature and room temperature appears to be between 45 and 55 cracks/in/ply. Thus, the fatigue crack saturation density is higher than that found during quasi-static loading (30-35 cracks/in/ply). The difference, also observed by Obst et al. [15], may be explained in several ways. One point that should be made is that the cracks in the fatigue specimens opened up more than the cracks in the quasi-static specimens and were easier to locate. The difference in the visibility of the cracks can be seen in edge replicas such as shown in Figure 13 for the quasi-static case and Figure 30 for the fatigue case. In fatigued specimens, the delaminations may have made it easier for the cracks to open. We may also speculate that the crack saturation density is greater for fatigue specimens than for quasi-static specimens because cracks have more opportunity to grow, particularly as the individual plies start to carry increasing loads.

In Figure 42, it can be seen that the crack saturation density for specimens aged hygrothermally for 12000 hours and then fatigued was actually notably lower than for their unaged counterparts. By the same arguments made for the moisture saturated specimen crack density data, this result represents a third indication that the fiber/matrix interface of the aged material may have been degraded.

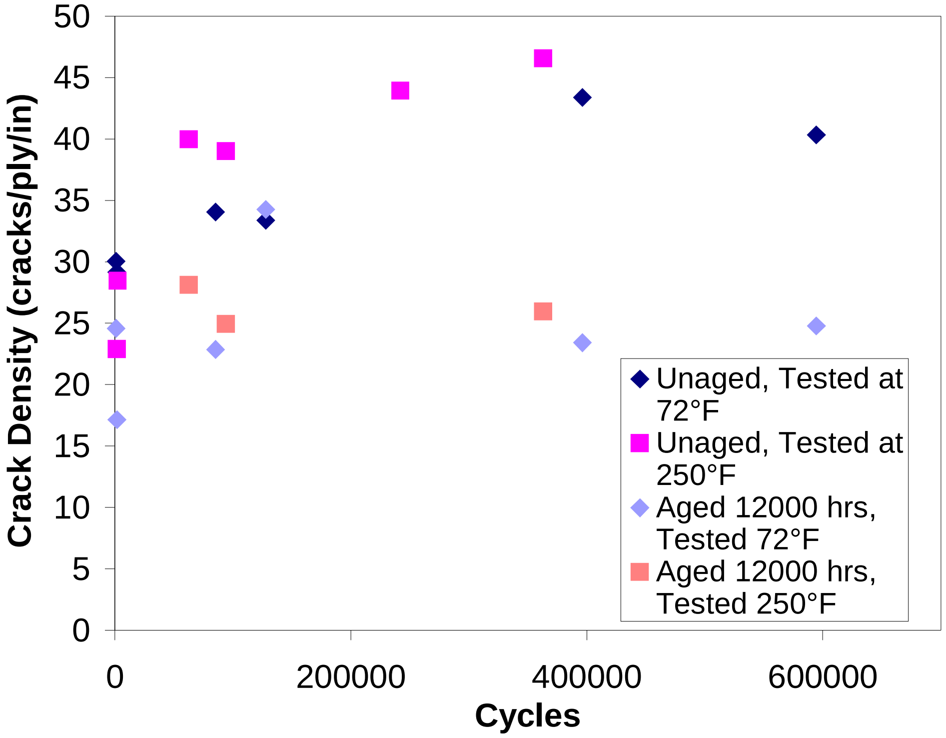

Figure 42: Crack densities of aged and unaged specimens at room temperature and elevated temperature as a function of fatigue cycles

Chapter 4 Analytical Methods and Results

4.1 Initial Stiffness Modeling of Woven Composites

An accurate model to predict initial properties of composite laminates can provide a critical first step towards minimizing the need for experimental testing and providing inputs for larger scale modeling (i.e., life prediction). The complicated architecture of woven composite laminates deserves attention in such modeling efforts. As discussed in Section 2.3, a variety of models with varying degrees of complexity exist. In this study, a model developed by Ishikawa and Chou [22] was used to predict the initial stiffness of the composite laminate.

In the "fiber undulation model", the following form of undulation is assumed for the fill thread (see Figure 43)

$$h_1(x) = \begin{cases} 0 & (0 \le x \le a_0) \\ \left[1 + \sin\left\{\left(x - \frac{a}{2}\right)\frac{\pi}{a_u}\right\}\right]\frac{h_t}{4} & (a_0 \le x \le a_2) \\ \frac{h_t}{2} & (a_2 \le x \le ng\frac{a}{2}) \end{cases} \tag{3}$$

where ng is the weave order (i.e., in this case, ng = 5). The shape of the warp thread is then

$$h_2(x) = \begin{cases} 0 & (0 \le x \le a_0) \\ \left[1 - \sin\left\{\left(x - \frac{a}{2}\right)\frac{\pi}{a_u}\right\}\right]\frac{h_t}{4} & (a_0 \le x \le \frac{a}{2}) \\ -\left[1 + \sin\left\{\left(x - \frac{a}{2}\right)\frac{\pi}{a_u}\right\}\right]\frac{h_t}{4} & (\frac{a}{2} \le x \le a_2) \\ \frac{h_t}{2} & (a_2 \le x \le ng\frac{a}{2}) \end{cases} \tag{4}$$

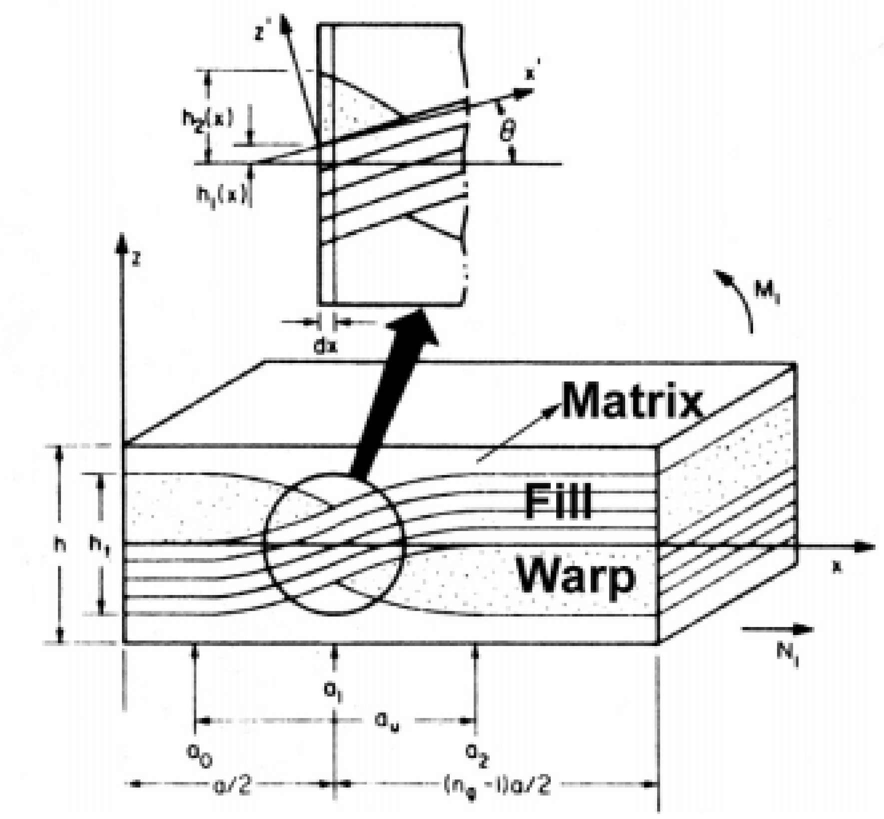

Figure 43: Fiber undulation representation [22]

The theory involved in the model is based on the classical laminated plate theory (CLT), where the constitutive Equations are given by

$$\begin{pmatrix} N_i \\ M_i \end{pmatrix} = \begin{bmatrix} A_{ij} & B_{ij} \\ B_{ij} & D_{ij} \end{bmatrix} \begin{pmatrix} \varepsilon_j^{0} \\ \kappa_j \end{pmatrix} \tag{5}$$

and

$$(A_{ij}, B_{ij}, D_{ij}) = \sum_{m-1}^{4} \int_{h_m -1}^{h_m} (1, z, z^2) Q_{ij} dz \tag{6}$$

The theory assumes that CLT is applicable to each infinitesimal piece of the model along the x-axis. Since experimental data show that the composite laminate undergoes little to no bending in tensile loading, the κ_j term in Eq. (5) is zero. In addition, since no moments are applied, the B matrix must be zero and the D matrix is not necessary for the tensile stiffness calculation. From Eq. (6), the A matrix for $0 \le x \le a/2$ is

$$\begin{aligned} A_{ij}(x) = & \int_{-h/2}^{h_1(x)-h_t/2} Q_{ij}^{M} dz + \int_{h_1(x)-h_t/2}^{h_1(x)} Q_{ij}^{F}(\theta) dz + \int_{h_1(x)}^{h_2(x)} Q_{ij}^{W} dz \\ & + \int_{h_2(x)}^{h/2} Q_{ij}^{M} dz \\ = & \; Q_{ij}^{M}(h_1(x) - h_2(x) + h - h_t/2) + Q_{ij}^{F}(\theta) h_t/2 + Q_{ij}^{W}(h_2(x) - h_1(x)) \end{aligned} \tag{7a}$$

Similarly, for $a/2 \le x \le ng\ a/2$, the A matrix is

$$A_{ij}(x) = -Q_{ij}^{M}(h_1(x) - h - h_2(x)) + Q_{ij}^{F}(\theta)(h_t/2) - Q_{ij}^{W}(h_2(x) - h_1(x) + h_t/2) \tag{7b}$$

In Eqs. (7a) and (7b), the superscripts M, F, and W stand for the matrix, fill, and warp threads, respectively. Moreover, the angle of the fill thread, θ, at a given x can be calculated as

$$\theta(x) = \arctan\left(\frac{dh_1(x)}{dx}\right) \tag{8}$$

Note that the model neglects the undulation of the warp thread, which is considered to run straight and transverse to the fill thread.

The averaged in-plane compliance of the section shown in Figure 43 under a uniformly applied in-plane stress is then defined as

$$\bar{a}_{ij}^{U} = \frac{2}{n_g a} \int_0^{n_g a/2} a_{ij}^{*}(x)dx \tag{9}$$

where the U denotes the undulation model and $a_{ij}^{*}(x)$ is the inverse of $A_{ij}(x)$. The integration in Eq. (9) must be performed numerically and inverted to obtain the plate stiffness of just the undulating portion. Such a stiffness value is sufficient for plain weave composites, but generally underpredicts the stiffness of satin weave composites because the model neglects the regions of straight thread surrounding the undulating region, as shown in Figure 44.

To account for the surrounding straight regions, the authors developed the “bridging model”. As shown in Figure 44, the hexagonal shape of the repeating unit of the satin weave is modified to a square shape for simplicity. The bridging model accounts for the idea that regions B and D in Figure 44 carry higher loads than region C and act as bridges for load transfer to regions A and E. It is also assumed that regions B, C, and D have the same averaged mid-plane strain.

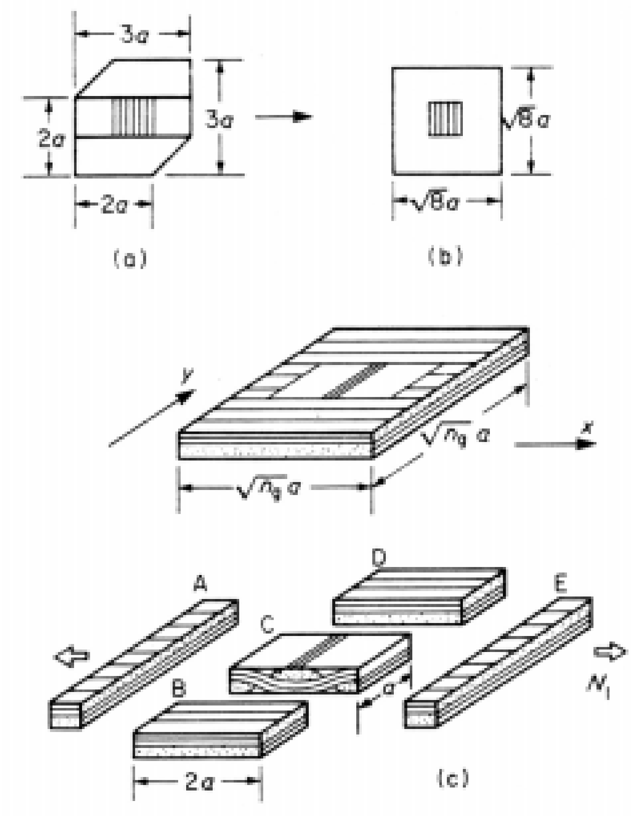

Figure 44: Bridging model representation [22]

The averaged stiffness constants for regions B, C, and D are then defined as

$$\overline{A}_{ij} = \frac{1}{\sqrt{n_g}}\left[(\sqrt{n_g} - 1)A_{ij} + \overline{A}_{ij}{}^{U}\right] \tag{10}$$

where A_{ij} is the average in-plane stiffness of an Eq.uivalent cross-ply laminate (in this case $[0/90]_{8s}$) and is given by

$$A_{ij} = (Q_{ij}{}^{W} + Q_{ij}{}^{F}(0))\frac{h}{2} \tag{11}$$

and $\overline{A}_{ij}{}^{U}$ is obtained by inverting the result of Eq. (9). Assuming that the total in-plane force carried by regions B, C, and D is equal to that carried by regions A and E, the average compliance for the entire satin weave plate is defined as

$$\bar{a}_{ij}^{*S} = \frac{1}{\sqrt{n_g}}[2\bar{a}_{ij}^{*} + (\sqrt{n_g} - 2)a_{ij}^{*}] \quad (12)$$

where $\bar{a}_{ij}^{*}$ is calculated by inverting Eq. (10). The final stiffness of the laminate is then calculated as $\frac{1}{\bar{a}_{11}^{*S}}$.

4.1.1 Model Inputs

For the material of interest in this study, the following parameter values were obtained from an edge replica as shown in Figure 45:

$h = h_t = 0.000389$ mm

$a_0 = 0$ mm

$a = a_u = a_2 = 0.0022$ mm

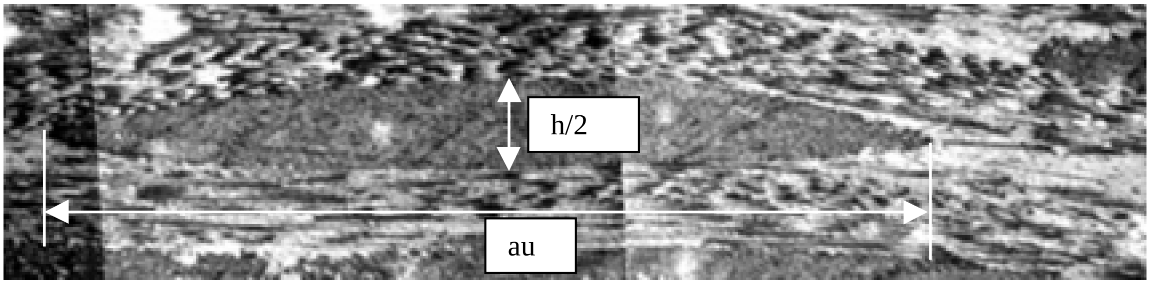

Figure 45: Edge replica showing actual material tow dimensions

For the fiber undulation portion of the model, ng equals two since only the undulation is considered; however, for the bridging model, the value of n_g represents the order of the weave, so in this case n_g is 5.

The reduced stiffness matrices for the fill and warp threads were determined by modeling the threads as individual unidirectional composites. The unidirectional composite properties were determined using micromechanics (i.e., Halpin-Tsai)

$$
\begin{aligned}
&E_1 = E_1{}^f v_f + E_1{}^m (1 - v_f) \\
&\nu_{12} = \nu_{12}{}^f v_f + \nu_{12}{}^m (1 - v_f) \\
&E_2 = \frac{E_2{}^m (1 + (\eta E)(\zeta E) v_f)}{1 - (\eta E) v_f} \\
&G_{12} = \frac{G_{12}{}^m (1 + (\eta G)(\zeta G) v_f)}{1 - (\eta G) v_f}
\end{aligned}
\tag{13a}
$$

where

$$
\eta_E = \frac{\left(\dfrac{E_2{}^f}{E_2{}^m} - 1\right)}{\left(\dfrac{E_2{}^f}{E_2{}^m} + \xi_E\right)}, \eta_G = \frac{\left(\dfrac{G_{12}{}^f}{G_{12}{}^m} - 1\right)}{\left(\dfrac{G_{12}{}^f}{G_{12}{}^m} + \xi_G\right)}
\tag{13b}
$$

and ξ_E=2 and ξ_G=1. The overall measured composite fiber volume fraction of 55% was used as the fiber volume fraction of the unidirectional composites. The matrix and fiber properties used are listed in Table 9.

Table 9: Fiber and matrix properties

	E1 (msi)	E2 (msi)	G_{12} (msi)	ν_{12}	ν_{23}
Fiber (AS-4)	34.1	24.6	8.0	0.25	0.27
Matrix (epoxy)	0.51	0.51	0.21	.35	0.35

The reduced stiffness matrices for the orthotropic laminate could then be calculated as

$$Q_{ij} = \begin{bmatrix} \frac{E_1}{1-\nu_{12}\nu_{21}} & \frac{\nu_{12}E_2}{1-\nu_{12}\nu_{21}} & 0 \\ \frac{\nu_{12}E_2}{1-\nu_{12}\nu_{21}} & \frac{E_2}{1-\nu_{12}\nu_{21}} & 0 \\ 0 & 0 & G_{12} \end{bmatrix} \tag{14}$$

where the matrix properties are substituted to obtain Q_{ij}^{M}, the fiber properties are substituted to obtain Q_{ij}^{F}, and Q_{ij}^{F} is transformed 90° to get Q_{ij}^{W}. In addition, the transformation matrix can be used to obtain $Q_{ij}^{F}(\theta)$.

4.1.2 Parameter Studies

Parameter studies are useful in optimizing processing techniques and material design. Table 10 contains the results from the model discussed above for different weave patterns. The calculated stiffness for the five harness satin weave (9.7 msi) turns out to be about 3% higher than the measured value (9.4 msi), which is quite reasonable. It should be noted, however, that the fiber volume fraction value used in the calculation may be questionable. Since the tows are being modeled as unidirectional composites, one might be tempted to use the tow fiber volume fraction (which would be considerably higher than the global fiber volume fraction) to calculate the ply properties. However, if the matrix that surrounds each lenticular tow is considered, the global fiber volume fraction appears to be the more reasonable value to use.

Table 10: Effect of weave pattern

Ng	**E_1 (msi)**
2	8.7
4	9.6
5	9.7
8	9.9
15	10.02

The calculated values shown in Table 10 reflect the fact that laminate stiffness increases for higher order weave patterns, approaching the cross-ply stiffness value calculated from CLT to be 10.1 msi. Despite the noticeable increase in stiffness, the only significant increase comes in going from the plain-weave architecture (ng = 2) to satin weave architectures ($ng \geq 4$). Such a result indicates that lower order weave patterns may be used to improve characteristics such as drapeability without significantly affecting stiffness.

Table 11 shows the effects predicted by the model of changing the aspect ratio, a/h, of the fiber tows. In this case, the value of the parameter h was modified to vary the aspect ratio, but the resulting stiffness change is equivalent to that resulting from changing the "a" parameter. As expected, increasing values of a/h result in higher stiffness since higher values of a/h correspond with less severe undulations. The calculations also show that, all else being equal, increases in h have little effect on stiffness for a/h greater than 6.

Table 11: Effects of changing tow height on laminate stiffness for $n_g = 5$

a/h	**E_1 (msi)**
3	9.1
6	9.7
9	9.9
12	10.0
15	10.02

4.2 Modeling of Diffusion in Damaged Composites

To describe the moisture uptake of a laminate containing cracks in directions both parallel and transverse to the axial direction, a modified version of the model developed by Roy [16] was implemented. The model makes use of continuum damage mechanics ideas combined with irreversible thermodynamics. Combining the chemical potential of moisture in a polymer

$$\mu = \rho_s \frac{\partial \phi}{\partial m} \tag{15}$$

with the conservation of mass in a unit volume of polymer

$$\frac{\partial m}{\partial t} = -\frac{\partial f_i}{\partial X_i}, \qquad \text{i = 1,3} \tag{16}$$

and assuming that the moisture flux, f_i (in the absence of temperature, stress, and damage gradients), for orthotropic symmetry is of the form

$$f_i = -D_i \frac{\partial \mu}{\partial X_i} \tag{17}$$

gives the governing equation for diffusion to be

$$\frac{\partial m}{\partial t} = \frac{\partial}{\partial X_i}\left(D_i \frac{\partial \mu}{\partial X_i} \right). \tag{18}$$

In the above Equations, ρ_s is the mass density of the polymeric solid, ϕ is Gibb's potential, and D_i is the diffusivity in a given direction, i. For the purposes of this study, consider the case where the only nonzero normalized stress is σ_{11}. Using a formulation for damage proposed by Talreja [29], the damage component corresponding to cracks in the transverse and axial directions, respectively, are

$$d_1 = \frac{\kappa_1(m,T) t_c^2 \delta_{11}}{t}$$

$$d_2 = \frac{\kappa_2(m,T) t_c^2 \delta_{22}}{t} \tag{19}$$

where 1 corresponds to transverse cracking, 2 corresponds to longitudinal cracking, and $\kappa(m,T)$ is an experimentally determined influence parameter that incorporates the constraining influence of moisture concentration (m), temperature (T), ply-orientation, and fiber architecture on crack opening displacement. In addition, t_c is the crack size, t is the total thickness of the laminate, and δ_{ii} (no summation) is the crack density, or number of cracks per length in the X_i direction. Using the form of Gibb's potential described by Roy then yields

$$\begin{aligned}\rho_s\phi &= \hat{C}_0 + \hat{C}_1\sigma_{11} + \hat{C}_2 d_{11} + \hat{C}_3 d_{22} + \hat{C}_4\sigma_{11}^2 + \hat{C}_5\sigma_{11}d_{11} + \hat{C}_6\sigma_{11}d_{22} \\ &+ \hat{C}_7 d_{11}^2 + \hat{C}_8 d_{22}^2 + \hat{C}_9 d_{11}d_{22} + \hat{C}_{10}\sigma_{11}^2 d_{11} + \hat{C}_{11}\sigma_{11}^2 d_{22} + \hat{C}_{12}\sigma_{11}d_{11}^2 \\ &+ \hat{C}_{13}\sigma_{11}d_{22}^2 + \hat{C}_{14}\sigma_{11}d_{11}d_{22} + \hat{C}_{15}d_{11}^2 d_{22} + \hat{C}_{16}d_{11}d_{22}^2\end{aligned} \tag{20}$$

From Eq. (15), the chemical potential is

$$
\begin{aligned}
\mu = \rho_s(&\frac{\partial \hat{C}_0}{\partial m} + \frac{\partial \hat{C}_1}{\partial m}\sigma_{11} + \hat{C}_1\frac{\partial \sigma_{11}}{\partial m} + \frac{\partial \hat{C}_2}{\partial m}d_{11} + \hat{C}_2\frac{\partial d_{11}}{\partial m} + \frac{\partial \hat{C}_3}{\partial m}d_{22} + \hat{C}_3\frac{\partial d_{22}}{\partial m} \\
&+\frac{\partial \hat{C}_4}{\partial m}\sigma_{11}{}^2 + 2\hat{C}_4\sigma_{11}\frac{\partial \sigma_{11}}{\partial m} + \frac{\partial \hat{C}_5}{\partial m}\sigma_{11}d_{11} + \hat{C}_5\left(\sigma_{11}\frac{\partial d_{11}}{\partial m} + d_{11}\frac{\partial \sigma_{11}}{\partial m}\right) \\
&+\frac{\partial \hat{C}_6}{\partial m}\sigma_{11}d_{22} + \hat{C}_6\left(\sigma_{11}\frac{\partial d_{22}}{\partial m} + d_{22}\frac{\partial \sigma_{11}}{\partial m}\right) + \frac{\partial \hat{C}_7}{\partial m}d_{11}{}^2 + 2\hat{C}_7 d_{11}\frac{\partial d_{11}}{\partial m} \\
&+\frac{\partial \hat{C}_8}{\partial m}d_{22}{}^2 + 2\hat{C}_8 d_{22}\frac{\partial d_{22}}{\partial m} + \frac{\partial \hat{C}_9}{\partial m}d_{11}d_{22} + \hat{C}_9\left(d_{22}\frac{\partial d_{11}}{\partial m} + d_{11}\frac{\partial d_{22}}{\partial m}\right) \\
&+\frac{\partial \hat{C}_{10}}{\partial m}\sigma_{11}{}^2 d_{11} + \hat{C}_{10}\left(\sigma_{11}{}^2\frac{\partial d_{11}}{\partial m} + 2d_{11}\sigma_{11}\frac{\partial \sigma_{11}}{\partial m}\right) + \frac{\partial \hat{C}_{11}}{\partial m}\sigma_{11}{}^2 d_{22} \\
&+\hat{C}_{11}\left(\sigma_{11}{}^2\frac{\partial d_{22}}{\partial m} + 2d_{22}\sigma_{11}\frac{\partial \sigma_{11}}{\partial m}\right) + \frac{\partial \hat{C}_{12}}{\partial m}\sigma_{11}d_{11}{}^2 \\
&+\hat{C}_{12}\left(2d_{11}\sigma_{11}\frac{\partial d_{11}}{\partial m} + d_{11}{}^2\frac{\partial \sigma_{11}}{\partial m}\right) + \frac{\partial \hat{C}_{13}}{\partial m}\sigma_{11}d_{22}{}^2 \\
&+\hat{C}_{13}\left(2d_{22}\sigma_{11}\frac{\partial d_{22}}{\partial m} + d_{22}{}^2\frac{\partial \sigma_{11}}{\partial m}\right) + \frac{\partial \hat{C}_{14}}{\partial m}\sigma_{11}d_{11}d_{22} \\
&+\hat{C}_{14}\left(d_{11}d_{22}\frac{\partial \sigma_{11}}{\partial m} + \sigma_{11}d_{22}\frac{\partial d_{11}}{\partial m} + \sigma_{11}d_{11}\frac{\partial d_{22}}{\partial m}\right) + \frac{\partial \hat{C}_{15}}{\partial m}d_{11}{}^2 d_{22} \\
&+\hat{C}_{15}\left(d_{11}{}^2\frac{\partial d_{22}}{\partial m} + 2d_{11}d_{22}\frac{\partial d_{11}}{\partial m}\right) + \frac{\partial \hat{C}_{16}}{\partial m}d_{11}d_{22}{}^2 \\
&+\hat{C}_{16}\left(d_{22}{}^2\frac{\partial d_{11}}{\partial m} + 2d_{11}d_{22}\frac{\partial d_{22}}{\partial m}\right))
\end{aligned}
\tag{21}
$$

Recognizing that, in this case, the chemical potential is a function of σ₁₁, d₁₁, d₂₂, T, and m gives:

$$
\frac{\partial \mu}{\partial X_i} = \frac{\partial \mu}{\partial m}\frac{\partial m}{\partial X_i} + \frac{\partial \mu}{\partial T}\frac{\partial T}{\partial X_i} + \frac{\partial \mu}{\partial \sigma_{11}}\frac{\partial \sigma_{11}}{\partial X_i} + \frac{\partial \mu}{\partial d_{11}}\frac{\partial d_{11}}{\partial X_i} + \frac{\partial \mu}{\partial d_{22}}\frac{\partial d_{22}}{\partial X_i} \tag{22}
$$

However, for the case of uniform damage, temperature, and stress distributions,

$$\frac{\partial \mu}{\partial X_i} = \frac{\partial \mu}{\partial m}\frac{\partial m}{\partial X_i} \tag{23}$$

and Eq.(17), for the unstressed case ($\sigma_{11} = 0$), becomes

$$\begin{aligned}
D_i \frac{\partial \mu}{\partial X_i} = \rho_s D_i [\{ & \frac{\partial^2 \hat{C}_0}{\partial m^2} + 2\frac{\partial \hat{C}_2}{\partial m}\frac{\partial d_{11}}{\partial m} + 2\frac{\partial \hat{C}_3}{\partial m}\frac{\partial d_{22}}{\partial m} + 2\hat{C}_9 \frac{\partial d_{11}}{\partial m}\frac{\partial d_{22}}{\partial m} \\
& + \hat{C}_2 \frac{\partial^2 d_{11}}{\partial m^2} + \hat{C}_3 \frac{\partial^2 d_{22}}{\partial m^2} + 2\hat{C}_7 \left(\frac{\partial d_{11}}{\partial m}\right)^2 + 2\hat{C}_8 \left(\frac{\partial d_{22}}{\partial m}\right)^2 \} + \{ \frac{\partial^2 \hat{C}_2}{\partial m^2} \\
& + 4\frac{\partial \hat{C}_7}{\partial m}\frac{\partial d_{11}}{\partial m} + 2\frac{\partial \hat{C}_9}{\partial m}\frac{\partial d_{22}}{\partial m} + 4\hat{C}_{15} \frac{\partial d_{11}}{\partial m}\frac{\partial d_{22}}{\partial m} + 2\hat{C}_7 \frac{\partial^2 d_{11}}{\partial m^2} + \hat{C}_9 \frac{\partial^2 d_{22}}{\partial m^2} \\
& + 2\hat{C}_{16} \left(\frac{\partial d_{22}}{\partial m}\right)^2 \} d_{11} + \{ \frac{\partial^2 \hat{C}_3}{\partial m^2} + 2\frac{\partial \hat{C}_9}{\partial m}\frac{\partial d_{11}}{\partial m} + 4\frac{\partial \hat{C}_8}{\partial m}\frac{\partial d_{22}}{\partial m} + 4\hat{C}_{16} \frac{\partial d_{11}}{\partial m}\frac{\partial d_{22}}{\partial m} \\
& + \hat{C}_9 \frac{\partial^2 d_{11}}{\partial m^2} + 2\hat{C}_8 \frac{\partial^2 d_{22}}{\partial m^2} + 2\hat{C}_{15} \left(\frac{\partial d_{11}}{\partial m}\right)^2 \} d_{22} + \{ \frac{\partial^2 \hat{C}_9}{\partial m^2} + \frac{\partial^2 \hat{C}_{15}}{\partial m^2} d_{11} \\
& + \frac{\partial^2 \hat{C}_{16}}{\partial m^2} d_{22} + 4\frac{\partial \hat{C}_{15}}{\partial m}\frac{\partial d_{11}}{\partial m} + 4\frac{\partial \hat{C}_{16}}{\partial m}\frac{\partial d_{22}}{\partial m} + 2\hat{C}_{15} \frac{\partial^2 d_{11}}{\partial m^2} + 2\hat{C}_{16} \frac{\partial^2 d_{22}}{\partial m^2} \} d_{11} d_{22} \\
& + \{ \frac{\partial^2 \hat{C}_7}{\partial m^2} + 2\frac{\partial \hat{C}_{15}}{\partial m}\frac{\partial d_{22}}{\partial m} + \hat{C}_{15} \left(\frac{\partial d_{22}}{\partial m}\right)^2 \} {d_{11}}^2 + \{ \frac{\partial^2 \hat{C}_8}{\partial m^2} + 2\frac{\partial \hat{C}_{16}}{\partial m}\frac{\partial d_{11}}{\partial m} \\
& + \hat{C}_{16} \frac{\partial^2 d_{11}}{\partial m^2} \} {d_{22}}^2] \frac{\partial m}{\partial X_i} \\
= {} & \overline{D}_i \frac{\partial m}{\partial X_i}
\end{aligned} \tag{24}$$

Assuming that the crack size t_c and crack densities δ_{11} and δ_{22} are not influenced by moisture absorption, from Eq. (19),

$$\frac{\partial}{\partial m}\left(\frac{\kappa_1 t_c{}^2 \delta_{11}}{t}\right)=\frac{t_c{}^2\delta_{11}}{t}\frac{\partial \kappa_1}{\partial m}$$

$$\frac{\partial}{\partial m}\left(\frac{\kappa_2 t_c{}^2 \delta_{22}}{t}\right)=\frac{t_c{}^2\delta_{22}}{t}\frac{\partial \kappa_2}{\partial m} \tag{25}$$

Substituting (25) into (24) and assuming κ_1 equals κ_2 (since for this case the weave is balanced and the material is transversely isotropic) yields

$$\begin{aligned}
\overline{D}_i = \rho_s D_i[&\frac{\partial^2 \hat{C}_0}{\partial m^2}+\{\frac{\partial^2 \hat{C}_2}{\partial m^2}\kappa+2\frac{\partial \hat{C}_2}{\partial m}\frac{\partial \kappa}{\partial m}+\hat{C}_2\frac{\partial^2 \kappa}{\partial m^2}\}\frac{t_c{}^2\delta_1}{t}+\{\frac{\partial^2 \hat{C}_3}{\partial m^2}\kappa+2\frac{\partial \hat{C}_3}{\partial m}\frac{\partial \kappa}{\partial m}\\
&+\hat{C}_3\frac{\partial^2 \kappa}{\partial m^2}\}\frac{t_c{}^2\delta_2}{t}+\{\frac{\partial^2 \hat{C}_9}{\partial m^2}\kappa^2+4\frac{\partial \hat{C}_9}{\partial m}\frac{\partial \kappa}{\partial m}\kappa+2\hat{C}_9\left(\frac{\partial \kappa}{\partial m}\right)^2+2\hat{C}_9\frac{\partial^2 \kappa}{\partial m^2}\kappa\}\frac{\delta_1\delta_2 t_c{}^4}{t^2}\\
&+\{\frac{\partial^2 \hat{C}_7}{\partial m^2}\kappa^2+2\hat{C}_7\left(\frac{\partial \kappa}{\partial m}\right)^2+4\frac{\partial \hat{C}_7}{\partial m}\frac{\partial \kappa}{\partial m}\kappa+2\hat{C}_7\frac{\partial^2 \kappa}{\partial m^2}\kappa\}\frac{t_c{}^4\delta_1{}^2}{t^2}+\{\frac{\partial^2 \hat{C}_8}{\partial m^2}\kappa^2\\
&+2\hat{C}_8\left(\frac{\partial \kappa}{\partial m}\right)^2+4\frac{\partial \hat{C}_8}{\partial m}\frac{\partial \kappa}{\partial m}\kappa+2\hat{C}_8\frac{\partial^2 \kappa}{\partial m^2}\kappa\}\frac{t_c{}^4\delta_2{}^2}{t^2}+\{\frac{\partial^2 \hat{C}_{15}}{\partial m^2}\kappa^3+6\frac{\partial \hat{C}_{15}}{\partial m}\frac{\partial \kappa}{\partial m}\kappa^2\\
&+6\hat{C}_{15}\left(\frac{\partial \kappa}{\partial m}\right)^2\kappa+3\hat{C}_{15}\frac{\partial^2 \kappa}{\partial m^2}\kappa^2\}\frac{t_c{}^6\delta_1{}^2\delta_2}{t^3}+\{\frac{\partial^2 \hat{C}_{16}}{\partial m^2}\kappa^3+6\frac{\partial \hat{C}_{16}}{\partial m}\frac{\partial \kappa}{\partial m}\kappa^2\\
&+6\hat{C}_{16}\left(\frac{\partial \kappa}{\partial m}\right)^2\kappa+3\hat{C}_{16}\frac{\partial^2 \kappa}{\partial m^2}\kappa^2\}\frac{t_c{}^6\delta_2{}^2\delta_1}{t^3}]
\end{aligned} \tag{26}$$

or

$$\overline{D}_i=[C_0+C_1\delta_1+C_2\delta_2+C_3\delta_1{}^2+C_4\delta_2{}^2+C_5\delta_1\delta_2+C_6\delta_1{}^2\delta_2+C_7\delta_1\delta_2{}^2] \tag{27}$$

Finally, from Eqs. (18), (25), and (26), the governing equation for an unstressed orthotropic laminate with uniform temperature and damage distributions becomes

$$\frac{\partial m}{\partial t}=\frac{\partial}{\partial X_i}[\rho_s D_i(C_0+C_1\delta_1+C_2\delta_2+C_3\delta_1^2+C_4\delta_2^2+C_5\delta_1\delta_2+C_6\delta_1^2\delta_2 +C_7\delta_1\delta_2^2)\frac{\partial m}{\partial X_i}] \tag{28}$$

Finding the coefficients C_0 through C_7 requires that eight different moisture diffusivities corresponding to each of 8 different states of laminate cracking be determined and substituted into Eq. (27). The eight equations would then have to be solved for the eight unknowns. However, if we neglect higher order terms ($\delta_1^2\delta_2$ and $\delta_2^2\delta_1$), Eq. (27) can be reduced down to containing only six constants. In addition, if we assume the effects of transverse cracks and longitudinal cracks to be identical (since axial and transverse mechanical properties were identical), the constants can be combined to give

$$\frac{\partial m}{\partial t}=\frac{\partial}{\partial X_i}\left[\rho_s D_i\left(C_0+C_1(\delta_1+\delta_2)+C_3(\delta_1^2+\delta_2^2)+C_4(\delta_1\delta_2)\right)\frac{\partial m}{\partial X_i}\right] \tag{28}$$

Thus, for the material and conditions discussed above, only one more diffusivity is needed to obtain the constants than for the single direction cracking case discussed by Roy.

The moisture diffusivity versus crack density data needed to find the constants in Eq. (28) and verify the method have not yet been collected.

4.3 Life Prediction

The life prediction methodology used in this study is one originally developed by Reifsnider and Stinchcomb [43] and further developed by Reifsnider and co-workers. Details of the method can be found in [36,37].

4.3.1 Critical Element Concept

Ideally, in applying this method, one would identify a representative volume element (RVE) which is subject to stress and damage states typical of the rest of the laminate. In addition, one may be able to divide the RVE into critical and sub-critical elements such that failure of the sub-critical elements does not lead to catastrophic failure of the laminate, but affects the stress-state of the critical element. The failure of the critical element then represents failure of the composite. If possible, the fatigue behavior of the critical and sub-critical elements would be considered separately and then combined to predict the fatigue behavior of the total laminate.

For instance, consider a [0/90] cross ply laminate. In this case, catastrophic failure is controlled by failure of the 0° plies, but failure of the 90° plies affects the stress state of the 0° plies. Thus, by characterizing the fatigue behavior of the 90° plies, the effect of the observed damage mechanisms and failure modes on the stress state of the 0° plies may be determined. Failure of the 0° plies, and therefore the composite laminate, can then be said to occur when the stress carried by the 0° plies reaches a critical level.

4.3.2 Residual Strength Concepts

According to the present modeling philosophy, the critical stress level discussed in the previous section would be the residual strength of the material. That is, failure of the laminate is assumed to occur when its residual strength degrades to the value of the maximum applied load. In addition, the residual strength is assumed to be a damage metric such that equivalent damage states are assumed to be represented by equivalent residual strengths. Based on kinetics arguments, Reifsnider [36] developed a damage evolution integral

$$\Delta Fr = -\int_{\tau_1}^{\tau_2} (1 - Fa)\, j\tau^{j-1} d\tau \tag{29}$$

by which the change in normalized residual strength (ΔFr) of a material may be calculated by implementing an appropriate failure criterion, Fa. In the case of mechanical fatigue, the characteristic time,τ, can be expressed as n/N where n is the number of fatigue cycles the material has undergone out of a total of N (usually fatigue life) cycles. Letting τ_1 equal zero and the initial normalized residual strength, Fr_1, equal one, Eq. (29) becomes

$$Fr = 1 - \int_{0}^{\tau} (1 - Fa(\tau))\, j\tau^{j-1} d\tau \tag{30}$$

Furthermore, for constant maximum amplitude fatigue, Fa may be considered to be constant, so

$$Fr = 1 - (1 - Fa)\tau^{j} \tag{31}$$

where j is an experimentally determined shape parameter.

4.3.3 Application

While the identification of an RVE and associated critical and sub-critical elements may be identified within the material system of interest in this study, the applicability of the ideas presented in Section 4.3.1 is difficult at best. For instance, the RVE may be considered to be the repeating unit of the weave, where the axial tows are the critical elements and the transverse tows and surrounding matrix are the subcritical elements. However, testing the critical and sub-critical elements independently seems virtually impossible. Thus, the critical element concepts were omitted from the present analysis.

Because the study was meant to examine the behavior of the material under a service condition which involved alternating periods of specific moisture and temperature conditions, it was thought that a similar paradigm to the critical element ideas presented above could be used to account for the different environments. The effect of each environmental condition on the residual strength of the material during fatigue was to be considered individually and then combined with the others to predict the fatigue behavior of the material under periodically changing environments. Since the experimental data for the unaged material reflected no significant and quantifiable effects of environment on its residual strength, this type of analysis was also omitted. Such an analysis may be possible for the material hygrothermally aged for 12000 hours since this material shows increased sensitivity to environment, but much of the needed experimental data has yet to be collected.

As a last resort, all the data from the testing of unaged material was used to obtain a single j value to be used in Eq. (31) along with the maximum stress failure criterion

$$Fa = \left(\frac{\sigma_{\max}^{applied}}{X_t} \right) \qquad (32)$$

In addition, τ was taken to be n/N where the estimated values of N shown in Table 6 and Table 7 were implemented. The value of j was chosen by determining the value that minimized the square of the error between calculated (from Eq. (31)) and measured values of normalized residual strength. The value of j was then determined to be 1.11. The calculated residual strength curves for material fatigued at different stress levels are shown in Figure 46. These curves are assumed to represent residual strength degradation for fatigue of unaged specimens under any of the considered environmental conditions since all the results were lumped together to determine j, and no significant change in residual strength was observed as a function of environment.

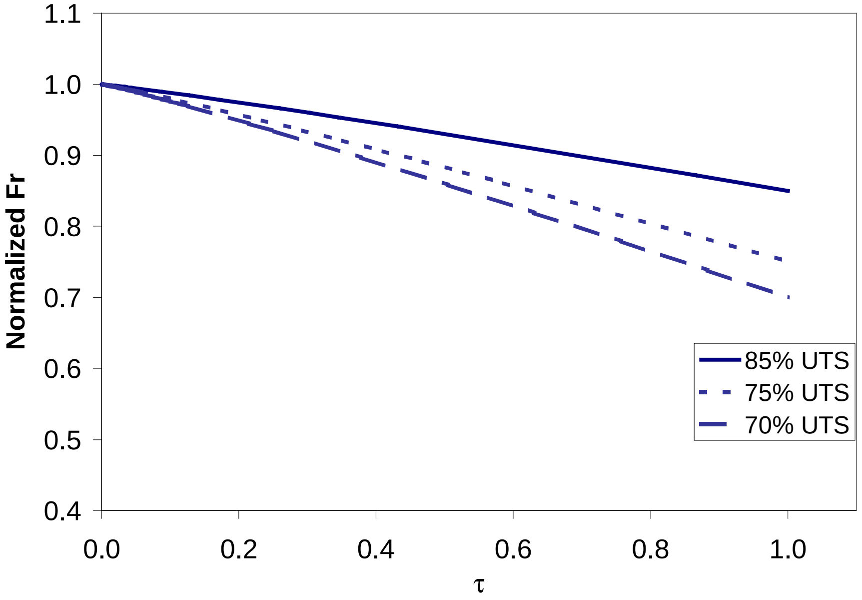

Figure 46: Calculated residual strength curves

Figure 47 gives an indication of how well the predicted normalized residual strength values matched the measured residual strength values. The closer the data points are to the line, the better the prediction. The results are as reasonable as possible given the scatter in the data.

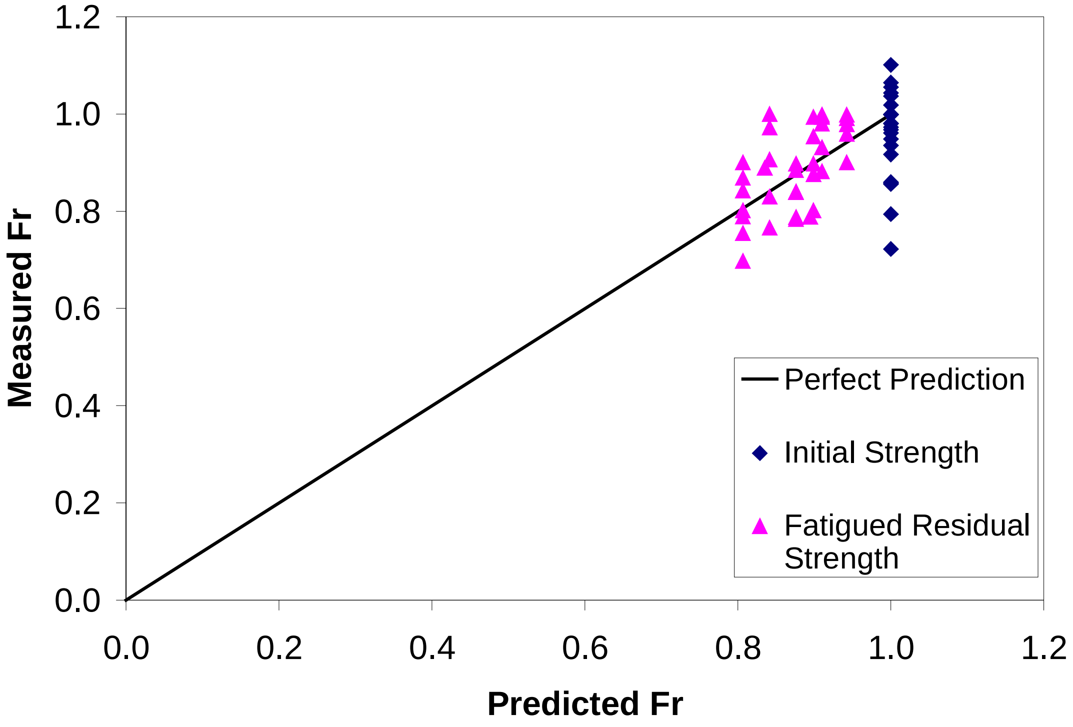

Figure 47: Comparison of measured versus predicted normalized remaining strength.

Chapter 5 Summary and Conclusions

The purpose of this chapter is to provide a synopsis of the findings of this research project.

5.1 Experimental Testing and Results

The experimental testing program in this project was constructed to obtain data necessary to study the damage progression in the graphite/epoxy woven laminate of interest and to obtain the fatigue life and residual strength data necessary to develop a residual strength based life prediction approach. The major findings of the experimental testing portion of the project are as follows.

Quasi-static tests show that:

- The ultimate tensile strength of unaged material is unaffected by the temperature and moisture conditions considered, namely 250°F (120°C) and saturation at 85% relative humidity at 85°F (29°C). The strength is also unaffected by aging the material under hygrothermal conditions for 12000 hours.
- The major damage mechanism resulting from quasi-static loading is cracking in the transverse tows. The crack density increases with loading, with each crack extending across a single transverse fiber bundle. In addition, the majority of the cracks appear relatively close to failure but do not reduce the elastic modulus.
- The nonlinearity (upward concavity) in the stress-strain curves indicates that the fiber bundles may undergo some straightening, resulting in stiffening of the laminate with loading. This straightening may be in line with the onset of gross transverse cracking, where the cracking relaxes the constraint on the axial tows.

Fatigue testing and residual testing showed:

- Fatigue life and residual strength of unaged material are, at best, minimally affected by the elevated temperature, moisture, or hygrothermal conditions imposed and stress levels considered. In addition, the shallow S-N and residual strength curves indicate that the material has a relatively high practical fatigue limit, and that fatigue failure is a sudden death event.
- Abnormalities in many of the specimens saturated for testing under the moisture condition rendered the affect of moisture saturation somewhat questionable.
- Room temperature residual strength testing of material aged for 12000 hours indicates no deviation in results from that of unaged material tested at room temperature. However, a small but noticeable increased level of degradation was found for aged material tested at elevated temperature over unaged material tested at elevated temperature.
- Residual stiffness measurements indicated that the material undergoes even less stiffness degradation than strength degradation, possibly due to the fiber bundle straightening.
- Damage progression during fatigue occurred in the following general order: transverse microcracking and delaminations around the fiber bundle undulation regions, longitudinal microcracking around fiber bundle undulation regions, growth of transverse cracks across the entire height of the transverse fiber bundle, and cross-ply like growth of edge and interply delamination. The rate at which the damage

progression occurred generally depended on the maximum fatigue stress amplitude and the corresponding fatigue life.

- Differences in the rate of damage progression from that of unaged room temperature specimens were observed in unaged elevated temperature specimens and aged room temperature and elevated temperature specimens in that increased levels of delamination were observed. These differences were manifested in dynamic stiffness loss curves. In addition, for aged specimens, the crack saturation density was much lower than that of the unaged specimens.

Aside from the factors already mentioned, other evidence that the integrity of the material was compromised by hygrothermal aging include:

- Observation of transverse microcracking at fiber undulation areas for material aged for 6000 hours and the additional observation of longitudinal microcracks in material aged for 12000 hours. These observations were made prior to mechanical loading of the material.
- Apparent higher moisture content of aged material over unaged material despite the increase in T_g and thermal degradation temperature of the laminate.

The latter result coupled with the lower crack saturation density of the aged, fatigued material and the higher fiber pullout in aged quasi-static specimens over unaged specimens, indicates that the aged material may have undergone some interfacial damage.

5.2 Analysis and Modeling

Efforts were made to model 1) initial laminate stiffness based on the fiber undulation and bridging models presented by Ishikawa and Chou [22], 2) moisture uptake of the laminate based on ideas developed by Roy [16], and 3) residual strength degradation based on ideas described by Reifsnider and co-workers [36,37] with the following results:

- Initial stiffness: the predicted stiffness of 9.7 msi agreed very well with the average measured value of 9.4 msi. Parametric studies showed that the order of the weave does not affect the stiffness significantly for $n_g \geq 4$. In addition, the aspect ratio of the fiber bundle length to the fiber bundle height also makes little difference for $a/h \geq 6$.
- Moisture uptake: a modified version of the model given by Roy [16] was developed to account for cracks transverse and parallel to the axial direction. Simplifying assumptions reduce the problem down to solving four Equations for four constants with the aid of four moisture uptake experiments in which the laminate is under a different damage state in each of the experiments. These experiments are currently under way.
- Residual strength: intentions to use the model as prescribed were limited by the complicated fiber architecture and lack of effect of the imposed temperature and moisture conditions on residual strength. A much simplified version of the model was used in which the room temperature, elevated temperature, and moisture testing results were combined to obtain a single residual strength prediction of the form

$$Fr = 1 - (1 - Fa)\tau^{j}$$

The parameter j was experimentally determined to be 1.11. Reasonable results were obtained.

5.3 Current Work

Currently, testing of aged material is still underway. Pending completion of the testing, conclusions will be drawn on the effects of aging on the material system. In addition, efforts are being made to study the effects of transverse and longitudinal cracking on the moisture uptake characteristics of the material. The results will be used to verify or refine the model discussed in Section 4.2.

5.4 Future Work Recommendations

The following represent suggestions for future work based on observations made during the present study:

- The fatigue behavior of the material at lower fatigue stress levels should be considered. While the residual strength modeling was meant to serve such purposes, the lack of residual strength changes with environment observed in experimental testing may be an artifact of the time periods involved. For instance, temperature and moisture are known to affect materials in a time-dependent manner, and the experimental data in this case suggests that at least temperature affects damage progression rate. Thus, it is reasonable to conjecture that differences in residual strength from that of material tested at room temperature may evolve with longer temperature exposure times. Such differences did not manifest themselves in the time periods involved in the present study in a conclusive manner. Consequently, the resulting residual strength predictions may overestimate the life of the material at elevated temperature for lower fatigue stress levels, where the temperature exposure time may be adequate to produce larger changes in residual strength. Studying the effects of environment at lower fatigue stress levels would thus provide more reliable and practical (since an aircraft engine is likely to operate at lower stress levels than the ones considered in this study) results by which to base material selection and modeling parameters.

- Although residual strength and stiffness were minimally affected by fatigue damage mechanisms, one would expect that events such as interfacial degradation and delamination would have a large effect on out-of-plane (i.e., shear and transverse) properties. Therefore, studying the degradation of shear and transverse properties during axial fatigue may prove useful (albeit difficult).
- Delamination should be included in the moisture diffusion modeling since the current study revealed that delaminations at the cross-over regions occurred prior to the onset of longitudinal cracking.
- While the case of fatigue in conjunction with hygrothermal cycling was considered in this study, a more practical situation should be considered where the fatigue cycling only takes place during the temperature portion of the hygrothermal cycle. This procedure represents a more realistic simulation of actual service conditions.
- The evaluation of the effects of moisture saturation and testing in humid conditions should be performed again in consideration of the material problems encountered in this study and consequential ambiguity of data.

References

1. Fujii, T., Amijima, S., and Okubo, K., “Microscopic Fatigue Processes in a Plain-Weave Glass-Fibre Composite,” *Composites Science and Technology*, Volume 49, No. 4 (1993), pp. 327-333.

2. Reifsnider, K. L., Schulte, K., and Duke, J. C., “Long-Term Fatigue Behavior of Composite Materials,” *Long-Term Behavior of Composites*, ASTM STP 813, T. K. O’Brien, Ed., American Society for Testing and Materials, Philadelphia, 1983, pp. 136-159.

3. Reifsnider, K. L., “Damage and Damage Mechanics,” *Composite Materials Series: Fatigue of Composites*, K. L. Reifsnider, ed., New York: Elsevier Science Publishers, Volume 4 (1990), pp. 11-77.

4. Takemura, K. and Fujii, T., “Fatigue Damage and Fracture of Carbon Fabric/Epoxy Composites Under Tension-Tension Loading,” *JSME International Journal*, Volume 37, Series A, No. 4 (1994), pp. 472-480.

5. Cler, S., “Fatigue Properties of Composite Materials Autoclave Processed From Carbon-Epoxy Woven Fabric Prepregs,”

6. Whitcomb, J.D., “Three-Dimensional Stress Analysis of Plain Weave Composites,” *Composite Materials: Fatigue and Fracture (Third Volume)*, ASTM STP 1110, T.K. O’Brien, ed., American Society for Testing and Materials, Philadelphia (1991), pp. 417-438.

7. Weitsman, Y., “Moisture in Composites: Sorption and Damage,” *Composite Materials Series: Fatigue of Composites*, K. L. Reifsnider, ed., New York: Elsevier Science Publishers, Volume 4 (1990), pp. 385-429.

8. Zhou, J. and Lucas, J. P., “Effects of Water on a Graphite/Epoxy Composite,” *Journal of Thermoplastic Composite Materials*, Volume 9 (1996), pp. 316-328.

9 DeNeve, D. and Shanahan, M. E. R., “Water Absorption by an Epoxy Resin and its Effect on Mechanical Properties and Infra-red Spectra,” *Polymer*, Volume 34 (1993), pp. 5099-5105.

10. Pipes, R. B., Vinson, J. R., and Chou, T. W., “On the Hygrothermal Response of Laminated Composite Systems,” *Journal of Composite Materials*, Volume 10 (1976), pp. 129-148.

11. Smith, L. V. and Weitsman, Y. J., “The Immersed Fatigue of Response of Polymer Composites,” *International Journal of Fracture*, Volume 82 (1996), pp. 31-42.

12. Serafini, T. T. and Hanson, M. P., “Environmental Effects on Graphite Fiber Reinforced PMR-15 Polyimide,” *Composites for Extreme Environments*, ASTM STP 768, N. R. Adsit, ed., American Society for Testing and Materials, 1982, pp. 5-19.

13. Shyprykevich, P. and Wolter, W., “Effects of Extreme Aircraft Storage and Flight Environments on Graphite/Epoxy,” *Composites for Extreme Environments*, ASTM STP 768, N. R. Adsit, ed., American Society for Testing and Materials, 1982, pp. 118-134.

14. Whiteside, J. B., DeIasi, R. J., and Schulte, R. L., “Distribution of Absorbed Moisture in Graphite/Epoxy Laminates After Real-Time Environmental Cycling,” *Long-Term*

Behavior of Composites, ASTM STP 813, T. K. O'Brien, ed., American Society for Testing and Materials, Philadelphia, 1983, pp. 192-205.

15. Obst, A. W., VanLandingham, M. R., Eduljee, R. F., Gillespie, J. W. Jr., Griesheim, G. E., and Tosi, K. F., "The Effect of Hygrothermal Cycling on the Microcracking Behavior of Fabric Laminates," *Technology Transfer in a Global Community International SAMPE Technical Conference*, Volume 28 (1996), pp. 994-1002.

16. Roy, S. and Xu, W., "Modeling of Diffusion in the Presence of Damage in Textile Composites," *Submitted to International Journal of Solids and Structures* (1999).

17. McLaughlin, P. V. D. Jr., McShane, H. A., Cochran, R., and Armstrong-Carroll, E., "Effects of High Heat on the Strength and Fatigue Life of Unidirectional Polymer-Matrix Composites," *Proceedings of the ASME Aerospace and Materials Divisions*, AD-Volume 51/MD-Volume 73 (1996), pp. 427-441.

18. Miyano, Y., McMurray, M. K., Enyama, J., and Nakada, M., "Loading Rate and Temperature Dependence of Flexural Fatigue Behavior of a Satin Woven CFRP Laminate," *Journal of Composite Materials*, Volume 28, No. 4 (1994), pp. 1250-1260.

19. Case, S. W., *Mechanics of Fiber-Controlled Behavior in Polymeric Composite Materials*, Ph.D. Dissertation, Virginia Polytechnic Institute and State University, (1996).

20. Whitcomb, J.D., "Comparison of Stress Concentrations in Plain and 8-Harness Satin Weave Composites", *Recent Advances in Mechanics of Aerospace Structures and Materials*, AD-Volume 56 (1998), pp. 23-32.

21. Tan, P., Tong, L., and Steven, G. P., “Modeling for Predicting the Mechanical Properties of Textile Composites-A Review,” *Composites Part A*, Volume 28A (1997), pp. 903-922.

22. Ishikawa, T. and Chou, T.W., “Stiffness and Strength Behavior of Woven Fabric Composites,” *Journal of Materials Science*, Volume 17 (1982), pp. 3211-3220.

23. Naik, N. K. and Shembekar, P. S., “Elastic Behavior of Woven Fabric Composites: I-Lamina Analysis,” *Journal of Composite Materials*, Volume 26 (1992), pp. 2196-2225.

24. Shembekar, P.S. and Naik, N.K., “Elastic Behavior of Woven Fabric Composites: II-Laminate Analysis,” *Journal of Composite Materials*, Volume 26, No. 15 (1992), pp. 2226-2246.

25. Walsh, T. J. and Ochoa, O. O., “Analytical and Experimental Mechanics of Woven Composites,” *Mechanics of Composite Materials and Structures*, Volume 3 (1996), pp. 133-152.

26. Naik, R., “Failure Analysis of Woven and Braided Fabric Reinforced Composites,” *Journal of Composite Materials*, Volume 29, No. 17 (1995), pp. 2234-2363.

27. Sendeckyj, G. P., “Life Prediction for Resin-Matrix Composite Materials,” *Composite Materials Series: Fatigue of Composites*, K. L. Reifsnider, ed., New York: Elsevier Science Publishers, Volume 9 (1994), pp. 53-78.

28. Talreja, R., “Life Prediction of Composite Structures By Damage Mechanics,” *Collection of Technical Papers AIAA ASME ASCE AHS ASC Structures, Structural Dynamics, and Materials Conference*, Volume 1 (1998), 345-351.

29. Talreja, R., “Damage Characterization By Internal Variables,” *Composite Materials Series: Damage Mechanics of Composite Materials*, R. Talreja, ed., New York: Elsevier Science Publishers, Volume 4 (1990), pp. 11-77.

30. Akshantala, N, V. and Talreja, R., “A Mechanistic Model for Fatigue Damage Evolution in Composite Laminates,” *Mechanics of Materials*, Volume 29 (1998), pp. 123-140.

31. Poursartip, A. and Beaumont, “The Fatigue Damage Mechanics of a Carbon Fiber Composite Laminate: II-Life Prediction,” *Composites Science and Technology*, Volume 25 (1985), pp. 283-299.

32. Yang, J.N., Yang, S.H., and Jones, D.L., “A Stiffness-Based Statistical Model for Predicting the Fatigue Life of Composite Laminates,” *Journal of Composite Technology and Research*, Volume 11, No. 4 (1989), pp. 129-134.

33. Whitworth, H. A., “Modeling Stiffness Reduction of Graphite/Epoxy Composite Laminates,” *Journal of Composite Materials*, Volume 21 (1987), pp. 362-372.

34. Schaff, J.R. and Davidson, B.D., “Life-Prediction Methodology for Composite Structures. Part I-Constant Amplitude and Two-Stress Level Fatigue,” *Journal of Composite Materials*, Volume 31, No. 2 (1997), pp. 128-157.

35. Yang, J.N and Liu, M.D., “Residual Strength Degradation Model and Theory of Periodic Proof Tests for Graphite/Epoxy,” *Journal of Composites*, Volume 11 (1977), pp. 176-203.

36. Reifsnider, K. L., “Use of Mechanistic Life Prediction Methods for the Design of Damage-Tolerant Composite Material Systems,” *Advances in Fatigue Lifetime Predictive*

Techniques: Second Volume, ASTM STP 1211, M. R. Mitchell and R. W. Landgraf, eds., American Society for Testing and Materials, Philadelphia (1993), pp. 3-18.

37. Case, S.W and Reifsnider, K.L., *MRLife 11: A Strength and Life Prediction Code for Laminated Composite Materials,* Materials Response Group, Virginia Polytechnic Institute and State University, Blacksburg, VA (1998).

38. *CRC Handbook of Chemistry and Physics*, 58th ed., CRC Press, Boca Raton, FL, Volume 27 (1977/78), p.**15**-25.

39. Shen, C. and Springer, G. S., “Moisture Absorption and Desorption of Composite Materials,” *Journal of Composite Materials*, Volume 10 (1976), p. 18.

40. Van Dreumel, W.H.M. and Kamp, J.L.M., “Non-Hookean Behavior in the Fibre Direction of Carbon-Fibre Composites and the Influence of Fibre Waviness on the Tensile Properties,” *Journal of Composite Materials*, Volume 11 (1977), pp. 461-469.

41. Highsmith, A.L., “The Effect of Delamination on the Behavior of Crossply Laminates,” *Mechanics of Composite Materials*, AMD Volume 92 (1988), pp.123-133.

42. O’Brien, T.K., “Characterization of Delamination Onset and Growth in a Composite Laminate,” *Damage in Composite Materials*, ASTM STP 775, K.L. Reifsnider, ed., American Society for Testing and Materials, Philadelphia (1982), pp. 140-167.

43. Reifsnider, K.L., and Stinchcomb, W.W., “A Critical-Element Model of the Residual Strength and Life of Fatigue-Loaded Composite Coupons,” *Composite Materials: Fatigue and Fracture*, ASTM STP 907, H. T. Hahn, ed., American Society for Testing and Materials, Philadelphia (1986), pp. 298-313.

Vita

Sneha Ramesh Patel

The author was born on April 6, 1974 to Ramesh and Hemlatta Patel in Danbury, Connecticut. She was raised in Danbury until the age of eight at which time the family moved to Ridgeway, Virginia. She graduated from Magna Vista High School in 1992 and obtained her B.S. degree in Engineering Science and Mechanics from Virginia Tech in 1996. She then accepted a position as a graduate research assistant working for Dr. Scott Case in the Materials Response Group at Virginia Tech.